Chapter 7
Probing Matter by Light

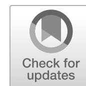

Mario Garcia-Lechuga, Javier Solis, and Jan Siegel

Abstract The success of ultrafast laser processing strategies to fabricate reproducible nanostructures below the diffraction limit was possible in part by understanding the complex material transformation pathways triggered by laser pulses. A continuously growing scientific community has focused on the development of experimental techniques, mostly based on probing matter by light, to unravel the underlying interaction mechanisms. Often supported by theoretical modelling, these techniques have greatly contributed to today's understanding of laser-matter interaction and enabled the identification of processing conditions that would have hardly been identified with empirical parameter scans. In this chapter, we review these light-based probing techniques, which interrogate in-situ the transient state of matter throughout its transformation from the initial state to the final state. Each technique is introduced and discussed in terms of its suitability for measuring certain transient changes induced, its spatial and temporal resolution, and is accompanied by results that illustrate its potential. Finally, a few examples of the applicability of some of these techniques in an industrial environment are given.

Keywords Time-resolved microscopy · Femtosecond laser · Pump-probe · Laser-matter interaction · Laser processing · LIBS

1 Introduction

Since the invention of lasers, they have become an essential tool both in scientific research and industrial development due to the unique properties of laser radiation. The way energy deposition with lasers can be controlled enables reaching interaction levels from the excitation of a single atom to the extreme relativistic regime. As a direct consequence, high-precision materials structuring is possible,

M. Garcia-Lechuga · J. Solis · J. Siegel (✉)
Laser Processing Group, Instituto de Óptica, IO-CSIC, Madrid, Spain
e-mail: mario.garcia.lechuga@csic.es; j.solis@csic.es; j.siegel@csic.es

© The Author(s), under exclusive license to Springer Nature Switzerland AG 2023

R. Stoian, J. Bonse (eds.), *Ultrafast Laser Nanostructuring*, Springer Series in Optical Sciences 239, https://doi.org/10.1007/978-3-031-14752-4_7

even at the nanoscale [1]. The spectrum of achievable laser-induced modifications is manifold, ranging from ablation (ejection of material) to subtler structural changes (melting, solidification, density changes, modifications in the crystal structure, phase segregation, etc.). Applications ranging from surface functionalization by nano- and microscale texturing to the generation of nanoparticles or the direct writing of photonic structures are thus feasible.

The physical mechanisms underlying these applications are as broad as the type of materials that can be processed by lasers. In each case, different processes will occur over a certain time scale leading to transient changes in the material properties, from the carrier excitation stage to the final chemical/morphological/structural changes induced. These transient changes very often manifest in changes of the optical properties, which enable them to be detected using light-based techniques.

In this first section, we will briefly describe the origin of the optical properties of materials, the mechanisms that cause optical changes upon laser irradiation, and the measurable optical parameters that enable the characterization of the transient and permanent modifications induced.

1.1 Brief Review of Light Interaction with Matter

Light propagation in materials can be described by Maxwell equations, no matter the complexity of solving them under many circumstances (anisotropic materials, nanomaterials, ultrashort-pulsed beams, nonlinearities, etc.). In this section, considering the context of laser processing, some simplifications are introduced. First, magnetic media are not considered; therefore, the wave equation for the electric field, $\overrightarrow{E}\ (x, y, z, t)$, is expressed as [2]

$$\nabla \times \left(\nabla \times \overrightarrow{E}\right) + \frac{1}{c^2}\frac{\partial^2 \overrightarrow{E}}{\partial t^2} = -\frac{1}{c^2\epsilon_0}\frac{\partial^2 \overrightarrow{P}}{\partial t^2} - \frac{1}{c^2\epsilon_0}\frac{\partial \overrightarrow{J}}{\partial t} \tag{7.1}$$

being c the speed of light in free space and ϵ_0 the permittivity of free space. The two terms on the right-hand side are called source terms and are related to the optical properties of the material. $\overrightarrow{P}$ is the polarization of the material, and the first term thus accounts for the light interaction with bound electrons (i.e., electrons in the valence band of a solid). $\overrightarrow{J}$ corresponds to the electric current density, and the second term is thus associated to the behavior of free electrons in the presence of an external electric field. Therefore, the first term is mostly relevant for nonconductive materials and the second one for conductive ones.

For the case of an isotropic medium, the propagation of a monochromatic electromagnetic wave can be expressed through a simplified wave equation

$$\nabla^2 \overrightarrow{E} = -\frac{\omega^2}{c^2} \cdot \epsilon\,(\omega) \cdot \overrightarrow{E} \tag{7.2}$$

with ω being the angular frequency of the E-field wave and ϵ the dielectric function of the material. This function is directly linked to the complex refractive index, $\widetilde{n}$, by the expression

$$\epsilon\,(\omega) = \tilde{n}^2 = (n + i\kappa)^2 \tag{7.3}$$

with n being the real part of the refractive index and κ the extinction coefficient of the material. In the frame of laser processing of materials, the extinction coefficient κ is a key factor, since it determines whether there is or not (linear) laser energy deposition in the material upon laser irradiation.

In a metal, light is absorbed by the free electrons via inverse bremsstrahlung. In a perfect dielectric material, there are no electrons in the conduction band to be accelerated by the field, and absorption is produced only when the photon energy is above the material bandgap (E_{gap}). This results in the generation of quasi-free electrons due to transitions from the valence to the conduction band. In narrow bandgap semiconductors (e.g., silicon, $E_{\text{gap}} = 1.1$ eV), absorption starts in the infrared region, while in wide band-gap semiconductors and dielectrics (optically transparent materials as sapphire,$E_{\text{gap}} = 8.8$ eV), absorption requires photon energies in the deep UV region. Additionally, absorption may occur via nonlinear ionization when irradiating with high-intensity laser pulses [3], something particularly relevant for laser processing of transparent materials. The required intensities should be above 10^{14} W/cm^2 [4], which are nowadays routinely achieved with commercial amplified ultrafast lasers (sub-picosecond pulse duration). From a theoretical point of view, the generation of free electrons by the strong-field ionization mechanisms (multiphoton absorption and tunneling ionization) is well described in the frame of the Keldysh formalism [5], described in more detail also in Chap. 1 of this book.

The indicated changes in the electron population in the energetic bands of the material due to light absorption has a direct impact on its optical properties, making the dielectric function to become time dependent, $\epsilon(\omega, t)$. As already mentioned, one of the most relevant transient effects of laser-matter interaction is the generation of free-carriers, which modifies the refractive index. This modification can be expressed by using the Drude-Lorentz model

$$\tilde{n}^2 = \tilde{n}_0^2 - \Delta\tilde{n}_{\text{Drude}}^2 \tag{7.4}$$

$\tilde{n}_0$ being the complex refractive index of the material before excitation and $\Delta\tilde{n}_{\text{Drude}}$ the contribution of the free electrons generated, which can be expressed as

$$\Delta\tilde{n}_{\text{Drude}}^2 = \frac{N_e}{N_c}\frac{1}{1 + i/\left(\omega\cdot\tau\right)} \tag{7.5}$$

with N_e being the free electron density, τ the scattering time of free electrons, and N_c the so-called critical electron density. This parameter is given by the expression $N_c = m^* \epsilon_0 \omega^2 / e^2$, with m^* being the reduced mass of the electron and e the charge

of the electron. This transient change in the optical properties caused by free-carrier generation is especially relevant in dielectrics. The excited material becomes absorbing due to the presence of free-carriers. The photo-generated free- or quasi-free-carriers may further absorb energy by inverse bremsstrahlung, thus increasing their kinetic energy. Once this energy becomes larger than the bandgap, the free electrons can inelastically collide with an electron in the valence band and promote it to the conduction band. This additional ionization mechanism is normally referred to as impact or avalanche ionization. The free electron dynamics, including both strong-field and impact ionization, can be modelled by using either single- or multi-rate equations [6, 7].

Along with the photo-generation of free electrons, there are other mechanisms that may induce transient changes in the optical properties upon excitation. Among them, the nonlinear Kerr effect triggers an instantaneous increase of the refractive index that is proportional to the intensity of the incoming laser pulse [8]. Additionally, the formation of self-trapped excitons (STEs) may take place, especially in materials with a small elastic constant, like fused silica and alkali halides. In STEs, excitons are strongly bound and localized near a single atom [9], although there is a certain controversy about their efficiency as an energy relaxation mechanism [10, 11]. Moreover, the elevated temperatures and pressures the material may experience upon laser exposure may also affect its optical properties [12]. Material heating, melting, flow, evaporation, re-solidification, and permanent structural or topographic changes will obviously affect optical properties. Finally, along with changes in the dielectric function, carrier relaxation may induce light emission from out-of-equilibrium states. Even at low excitation levels, the spectral and intensity analysis of the emitted light can be of relevance for accessing the composition and thermodynamic state of the material upon irradiation [13]. At higher intensities, plasma (light) and particle emission analysis provides a wealth of information regarding the interactions, as discussed in more detail in Sect. 2.1.

1.2 Concept of Probing Matter by Light

The characterization of permanent optical changes in the processed material allows accessing in a simple way modifications that can be of scientific or industrial interest. They may include subtle changes in the surface topography or much stronger ones such as ablated craters which provide information directly related to the processing quality. In this section we focus on the concept of optical probing techniques for which the detected light wavelength is the same as the incident probe wavelength. Other powerful probing techniques do not belong to this category, such as Raman spectroscopy techniques, which are discussed, for instance, in [14].

Optical microscopy is arguably the simplest technique for a quick and visual analysis of the produced changes. Among the different optical microscopy modalities, bright-field microscopy is the most commonly used one. Depending on the illumination configuration, it allows assessing the material reflectivity and

transmissivity. These two macroscopic magnitudes, reflectivity and transmissivity, are essential to retrieve the optical changes produced after excitation. Reflectivity, when illuminating the surface at normal incidence, is given by

$$R = \left| \frac{\tilde{n}_2 - \tilde{n}_1}{\tilde{n}_2 + \tilde{n}_1} \right|^2 \tag{7.6}$$

with $\tilde{n}_1$ being the complex refractive index of the medium of incidence (normally air: $\tilde{n}_1 \approx 1$) and $\tilde{n}_2$ the complex refractive index of the material under study. Reflectivity depends both on the real part and imaginary part (extinction coefficient) of the refractive index. The separation of both contributions to the complex refractive index from a reflectivity measurement at a single angle of incidence is not possible. However, by combining reflectivity and transmission measurements, this difficulty can be solved since transmissivity is given by the attenuation of light propagating through the material (only κ dependent). This behavior is mathematically described by the Beer-Lambert law:

$$I(z) = I_0 \cdot e^{-\alpha z} \tag{7.7}$$

where I is the intensity of the light propagating inside the material along the z-axis, I_0 is the intensity at the surface, and α is the absorption coefficient, defined as $\alpha = 2\omega\kappa/c$. The inverse of the absorption coefficient is the so-called skin penetration depth ($\delta = \alpha^{-1}$).

This methodology to retrieve n and κ is limited to materials with low attenuation or thin layer thickness. An alternative to fully retrieve the dielectric function is the use of ellipsometry, which measures the change of polarization upon reflection at different angles of incidence for a single or multiple wavelengths. From the measured changes (and in most cases supported by additional modelling), it is possible to invert the Fresnel equations [2] and to obtain the values of n and κ at the single or multiple wavelengths (spectroscopic ellipsometry) used.

In the above description, the analysis of light properties after interacting with a material has been focused only on the analysis of changes in the amplitude of the illumination beam, either in reflection or in transmission. The analysis of phase shifts in the light-material interaction provides an additional route to access to the optical properties of the material. The characterization of the phase is achieved by using interferometric layouts that are described next.

Figure 7.1 shows several images of modified regions produced upon exposure to a single femtosecond laser pulse above the modification threshold. The images were recorded in reflection illuminating with a blue LED ($\lambda = 460 \pm 25$ nm). The images show, along with an ablation crater and surrounding material debris, a set of contrasted annular rings within the irradiated region. This optical effect is due, as sketched on the right-hand side of the figure, to an interferential phenomenon (Newton's rings) arising from the presence of a thin heat-affected layer underneath the crater. The illumination beam is reflected both at the top and bottom interface of

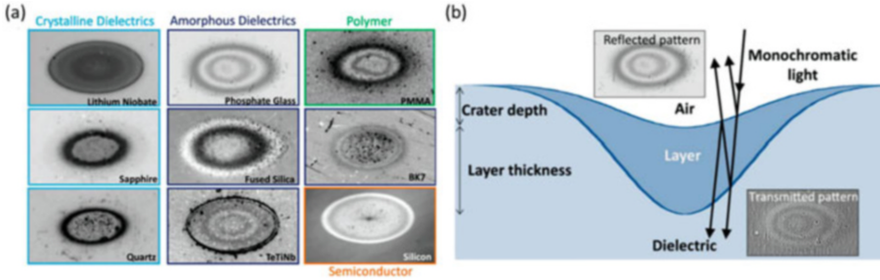

Fig. 7.1 (**a**) Optical microscopy images at 460 nm illumination wavelength of irradiated regions (ultrashort laser pulse at 800 nm) for different materials. (**b**) Scheme of the multilayer interference system in the irradiated region, where examples of the images in reflection and transmission are shown. (Adapted with permission from [16] © The Optical Society)

this layer, introducing an optical path difference (OPD) between the two reflected beams. The OPD is proportional to the real part of refractive index (n_l) and the thickness of the layer (d_l):

$$\text{OPD} = 2 \cdot n_l \cdot d_l \tag{7.8}$$

The factor of 2 accounts for the full round trip of the beam reflected at the bottom interface of the layer. Constructive interference occurs when the two beams are in phase (a phase difference equal to 2π or a multiple), which occurs when the OPD is equal to the illumination wavelength or a multiple of it. Therefore, by counting the number of Newton's rings and their corresponding position, it becomes possible to characterize the optical thickness ($n_l \cdot d_l$) of the layer at each position. The deconvolution of index and depth requires an additional analysis of the optical contrast of the rings and a comparison with simulations based on the optical behavior of thin films [15].

The characterization of the OPD in different regions of the irradiated zone allows thus extracting important properties of the modified material. This characterization is especially relevant when the induced modifications show low optical contrast (small changes in reflectivity and transmission). The group of techniques specially designed for characterizing the spatial distribution of the OPD are usually referred to as quantitative-phase microscopy. The usual configuration is based on a Mach-Zehnder interferometer, as sketched in Fig. 7.2a, in which the interference pattern generated by the phase difference of a reference beam and a beam traversing the sample is imaged onto a charge-coupled device (CCD) camera. This technique (in transmission configuration) requires the sample to be transparent at the illumination wavelength. In the example shown in Fig. 7.2, infrared light was used to record the changes induced after irradiation of a silicon sample [17]. Figure 7.2b shows the differences between a conventional intensity image (at the top) and a phase image

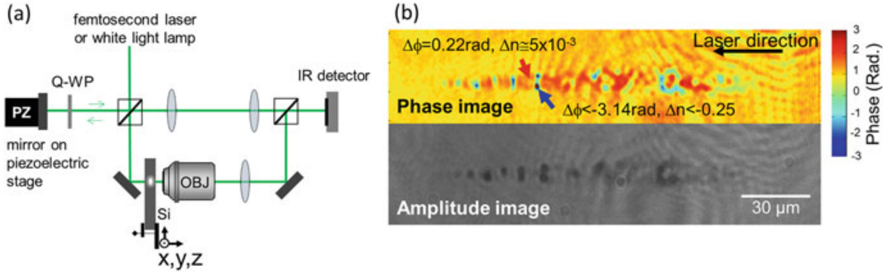

Fig. 7.2 (**a**) Schematic view of an experimental arrangement for quantitative-phase microscopy with infrared illumination. (**b**) Comparison between an amplitude image (top) and a phase image (bottom) of laser-generated microstructures inside a silicon sample. The regions marked with colored numbers correspond to positive (1 and 3) and negative (2) phase shift values. Provided by authors of [17]

(at the bottom). The phase image allows observing negative or positive phase-shift regions that can be respectively associated to densified or porous regions.

An additional and extremely useful interferometric technique is the so-called white light interference microscopy, or simply optical profilometry. This technique uses an interferometric microscope objective (Mirau objective), in which an interference pattern is formed because of the OPD between a reference beam and the beam reflected at sample surface. By unwrapping the phase-shift image, information about the surface topography with nanometric depth resolution can be extracted.

In summary, in this section we have presented different optical methods that allow accessing the changes produced in the material. The exemplified changes here are of permanent nature, but, as already indicated, they have their origin in transient phenomena (free electron generation, material melting, etc.). Thus, the use of techniques like the ones described here and adding temporal resolution capabilities enables the characterization of transient phenomena that eventually lead to the final material modification.

2 In-Situ Probing Technique

As indicated in Sect. 1.2, the concept underlying the use of optical probes to analyze light-matter interaction is using a secondary, weak light source (probe beam) to interrogate the optical properties of the material irradiated by a high-intensity (pump) laser pulse. This can be done using experimental layouts with spatial and/or temporal resolution. In the spatial case, this provides information about the optical properties of the material modified by the laser or the role of the local fluence of the pump laser in the process. In the temporal one, we acquire, for instance, information regarding the electron density evolution and the eventual structural changes induced upon carrier relaxation. In what follows, we

will make a somewhat artificial distinction between what we will call "real-time optical measurements" with ns (and sub-nanosecond) resolution and "time-resolved ultrafast optical measurements" with ps and fs resolution.

In the former, ("real-time techniques") we have access to the evolution of an optical property of the irradiated surface by using a continuous or relatively long pulsed optical probe beam and a sufficiently fast recording device (i.e., fast photodiode plus oscilloscope). Therefore, single pulse events can be recorded at once over a pre-established temporal window, no matter if the material undergoes a permanent transformation. This approach can be performed by using either point like probes (i.e., the probe light beam is focused inside a larger pump laser excited region) or image-based techniques (see Sect. 2.6 on ultrafast continuous imaging (*UCI*) techniques). In the second type ("time-resolved"), the surface is excited multiple times and interrogated with a pulsed optical probe to reconstruct the evolution of the optical property by scanning the temporal delay between the pump and the probe pulses. The temporal resolution of the measurement will be given by the width of the probe pulse (in most cases). If the material does not return to its initial state upon irradiation, the temporal reconstruction of the property of interest (i.e., reflectivity) makes it necessary to move the sample to a fresh region before each new pump laser pulse exposure.

The use of optical probes to analyze the temporal evolution of the laser-excited material is nearly as old as lasers are. Most likely, the first "real-time reflectivity measurements" performed upon laser excitation of a solid were reported in 1964 by researchers from the Hughes Aircraft Company [18]. They measured the temporal evolution of the reflectivity of several semiconductors (Ge, Si, InP, etc.) excited by single ns ruby laser pulses. Figure 7.3 (left) shows the experimental setup they used. Apart from the type of photodetectors used (photomultiplers), the layout has not changed much since then for this type of measurements. Interestingly, the authors of this work were not that much interested in the structural changes induced in the material but in the use of crystalline semiconductors as passive Q-switch elements in a pulsed laser cavity. The measured reflectivity evolution for the case of Ge is shown at the right of the figure, showing a reflectivity plateau for fluences above ~0.3 J/cm^2 that nowadays we would identify as laser-induced surface melting.

Since the publication of this early work, many research papers have reported on the temporal evolution of the optical properties of laser-excited materials in a variety of experimental configurations, using different interrogation parameters (reflectivity, transmission, luminescence, intensity, phase, refractive index, linear and nonlinear susceptibilities, etc.). In this section, we will review a number of them, including both point-probing (Sects. 2.2 and 2.3) and image-based (Sects. 2.4, 2.5, and 2.6) techniques. An initial sub-section devoted to laser-induced breakdown spectroscopy (Sect. 2.1) has been included, as it can be considered as a special class, a "self-probing" technique.

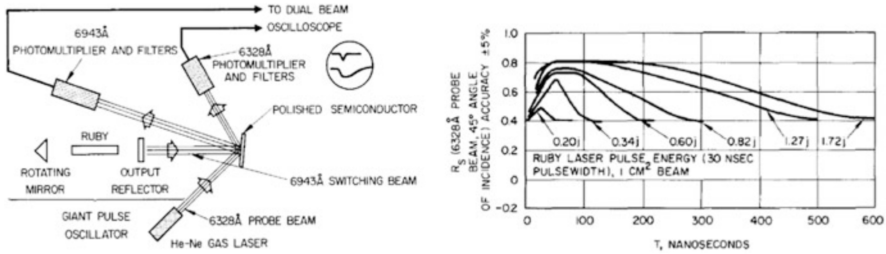

Fig. 7.3 (Left) Experimental apparatus for measuring the temporal evolution of the reflectivity of a switched semiconductor. (Right) Time dependence of the reflectivity R_s of mechanically polished Ge excited by a giant (30 ns) ruby laser pulse. (Reprinted from [18] with the permission of AIP Publishing)

2.1 Self-Probing: Laser-Induced Breakdown Spectroscopy

Laser-induced Breakdown Spectroscopy (LIBS) is a powerful optical technique for noncontact, remote analysis of the chemical composition of materials. The concept is based on irradiating the specimen of interest with a high-energy laser pulse and measuring the emission spectrum of the laser-induced ablation plasma formed near the material surface, which contains the fingerprint of the elemental composition. The history of LIBS, reviewed in detail in the excellent book by Cremers and Radziemski [19], began almost immediately after the invention of the laser. In 1963, in Debras-Guedon and Liodec published the first analytical use of lasers for spectrochemical analysis of surfaces [20]. Soon after, Runge et al. published a work employing a pulsed laser for direct excitation of steel, reporting a linear relationship of the nickel and chromium content with the intensities of the corresponding characteristic emission line, which demonstrated the potential of the technique of quantitative analysis via calibration [21]. Time-resolved studies of the emission spectra appeared soon after, which aided in the discrimination against bremsstrahlung, featuring a continuous spectrum. While in the early days such measurements were quite complex, the enormous progress in detector development, offering gated, intensified charge-coupled devices (ICCDs) or electron-multiplying CCDs (EMCCDs), greatly contributed to the progress in LIBS. Since the early 1990s, the scientific activity in the field has been (and still is) rising exponentially. One of the main reasons is the strong interest for a variety of industrial sectors, as detailed in [22].

It needs to be stressed here that it is not only the composition of the material of interest that can be extracted by this technique. LIBS, with its different modalities, constitutes a powerful tool for visualizing a wealth of different laser-matter interaction processes and has the ability to quantify numerous properties of the laser-generated plasma. Thanks to this ability, it can be considered a self-probing technique, that is, the same laser pulse that interacts with the material is used to probe the generated plasma by exciting it for spectral measurements. In the

following sections, a brief summary of the most important LIBS-based methods to quantify the properties of the ablation plasma is given.

2.1.1 Determining Electron Densities of a Laser-Induced Ablation Plasma

The dominant contributions to line broadening in a LIBS plasma are the Doppler effect and the Stark effect. The Doppler width $\Delta\lambda_D$ of an emission line λ_0 depends only on the absolute temperature T and the atomic weight M of the emitting species, according to the following equation [19]:

$$\Delta\lambda_D = \left(8k_BT * \ln 2/Mc^2\right)^{1/2}\lambda_0 \tag{7.9}$$

with k_B being the Boltzmann constant. In most cases of laser-produced plasmas, Doppler broadening is much smaller than broadening by the Stark effect, which is caused by collisions of the emitting species with electrons, and to a lesser extent by collisions with ions. Measuring stark-broadened line widths $\Delta\lambda_S$ can be used under certain conditions to calculate the electron density N_e in plasmas according to the following relation [23]:

$$\Delta\lambda_S = 2W \times \left(N_e/10^{16}\right)[\text{Å}] \tag{7.10}$$

where W is an electron impact parameter, which is a weak function of the temperature and only changes by a factor less than 2 over the temperature range 10.000–80.000 K. It should be noted that the FWHM line width $\Delta\lambda_S$ in Eq. (7.10) is given in Å and N_e in cm^{-3}. However, in the case of strong emission lines, an additional line-width broadening mechanism is often present, which is self-absorption of the light emitted from one atomic species and re-absorbed by another species. This effect causes an overestimation of the electron density but can be detected by a careful analysis of the line shape, which features a change in the spectral line shape and often take the form of a top-hat-shaped profile or even central dip. Since self-absorption severely affects the results obtained from plasma analysis, for precision studies, it is recommendable to perform them only on optically thin plasmas, where the emitted radiation traverses and escapes from the plasma without significant absorption or scattering.

2.1.2 Thermodynamic Equilibrium and Determining Electron Temperature

An important condition for being able to determine other plasma properties, such as electron speeds or populations of energy levels, is the presence of thermodynamic equilibrium. Only then, these properties can be described through the concept of temperature, which is accessible to LIBS. However, this condition is rarely fulfilled

for the entire lifetime of the plasma or for its complete spatial extension. Therefore, the concept of local thermodynamic equilibrium (LTE) has been introduced, which reduces this requirement to a small region. LTE can typically be assumed after a certain time, when a sufficient number of collisions have occurred to thermalize the plasma [19]. Once it can be assumed that LTE exists, the distribution of several quantities depends only on the electron temperature T_e of the ablation plasma, which can be determined by measuring the ratio of two line intensities from successive ionization stages of the same element [23]. From LIBS measurements it is also possible to determine temperatures of atom, ions, and the ionization equilibrium, as well as vibrational and rotational temperatures [19].

2.1.3 Temporally and Spectrally Resolved Imaging of Laser-Induced Plasmas

In view of the space constraints of this section, we would like to give just a single example for an experimental LIBS configuration and results obtained, reported by our group [24]. It is by no means representative or provides the most groundbreaking results but shows a combination of a conventional point-probing LIBS configuration with a time-resolved imaging configuration to provide temporal, spectral, and spatial information. The basic principle of the setup (sketched in Fig. 7.4a) consists of an ArF excimer laser (193 nm, 20 ns) incident at an angle on the target of interest, which is placed in a vacuum chamber with controlled gas pressure such that the ablated material (electron plasma, neutrals, ions) can expand from the surface. A 4f imaging system is installed in order to project the ablation plume onto the entrance slit of an imaging spectrograph, whose exit plane is recorded by a gated ICCD camera with adjustable exposure time (down to 30 ns).

The purpose of the periscope is to rotate the plume image in such a way that the expansion axis lies along the slit axis, thus preserving this spatial information as the vertical direction of the recorded image. The horizontal axis corresponds to the wavelength of the emitted light, dispersed by the diffraction grating inside the spectrograph. This technique has been applied to the study of the ablation and expansion dynamics of several materials at different ambient gas pressures with some results being shown in Fig. 7.4b–e) [24–26].

2.2 Real-Time Point-Probing with ns and Sub-ns Temporal Resolution

Before describing ultrafast resolution point-probing techniques in Sect. 2.3, it is worth taking a look at their lower-resolution antecessors, "real-time" optical measurements" with ns (and sub-nanosecond) resolution. In this respect, it should be noted that well before the successful development of the first solid state, chirped

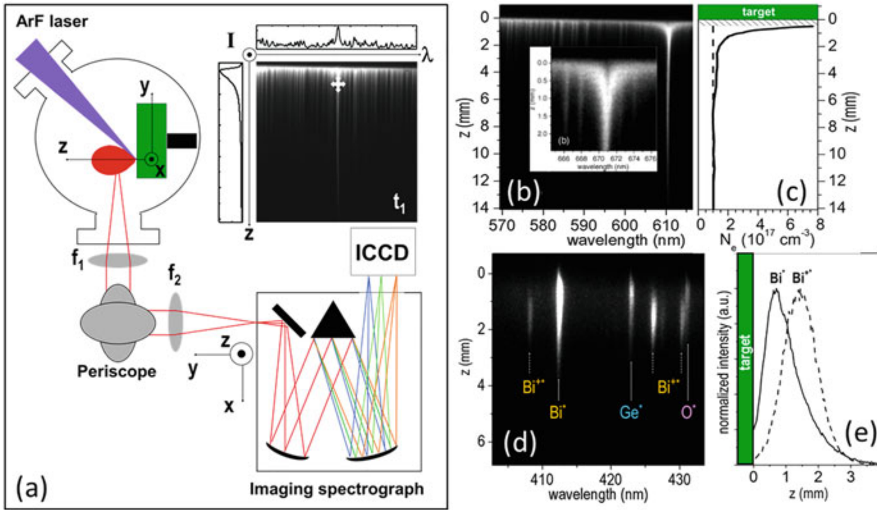

Fig. 7.4 (**a**) Experimental setup for spatial-spectral imaging of laser-induced plasmas with temporal resolution. (**b**) Time-integrated spatial-spectral image of the expanding $LiNbO_3$ plasma in vacuum, obtained by irradiating the target with a single-laser pulse. (**c**) Electron density N_e extracted from the 610.3 nm line in (**b**) as a function of distance z to the target. The shaded area in (**b**) very close to the surface (0.5–0 mm) indicates the region of self-absorption. (**d**) Time-gated ($\Delta t = 100$ ns, $t = 200$ ns) spatial-spectral image of the expanding plasma obtained by irradiating a $Bi_{12}Ge_1O_{20}$ target. (**e**) Transient spatial distributions of Bi neutrals (Bi* line at 412.2 nm) and Bi ions (Bi^{+*} line at 425.9 nm) extracted taken from (**d**). (Reprinted with permission from [24] © Elsevier)

pulse fs-laser amplifiers based on Ti:Sapphire crystals [27] for materials processing applications, ns laser lasers were routinely used for semiconductors processing [28, 29].

The first works on laser annealing of crystal damage in ion-implanted semiconductors date from the late seventies [30, 31]. The physical mechanisms underlying this process were the subject of an intense debate in the subsequent years. This debate boosted an enormous amount of experiments aimed at clarifying the role of carrier excitation and relaxation in the structural transformations induced in semiconductors upon short pulse (typically ns) laser irradiation. Their common denominator was the determination in "real time" of the temporal evolution of a given material property upon irradiation. Among them, experiments involving optical probes were particularly successful and included reflectivity [32, 33], reflectivity at multiple wavelengths [34], transmission [35], Raman [36], interferential [37], photoluminescence (self-probing) [38], and ellipsometry measurements [39]. Although not strictly "optical," ns-resolution "real-time" measurements using a point-probing scheme were carried out by using electron [40] or X-ray beams for diffraction [41] or absorption measurements [42]. Around the mid-1980s, it was more or less generally recognized that ns laser-induced annealing of semiconductors

was mediated by the formation of a thermal molten layer at the material surface that propagated inward, leading to the redistribution of ion-implanted dopants. This brief overview on early “real-time optical” point-probing measurements would not be complete without mentioning that electrical probe measurements [43, 44] were, along with ultrafast time-resolved measurements (Sect. 2.3), crucial in elucidating the controversy between the thermal [45, 46] and plasma models [47, 48] for laser annealing with ns-laser pulses. Obviously, the references above quoted are far from being an exhaustive selection since more than 1400 research papers on laser annealing of semiconductors were published just from 1978 to 1988.

In the subsequent years, real-time ns-resolution optical measurements were also crucial in the analysis of the variety of solidification scenarios that appear when ns and ps laser pulses interact with semiconductors, especially in thin film configuration (either amorphous or crystalline) on substrates with different thermal conductivities. Interfacial amorphization [49], inhomogeneous melting [50], bulk amorphization [51], surface-initiated solidification [52, 53], bulk solidification and explosive crystallization [54], propagation of molten buried layers [55], and recalescence phenomena [56] upon ns and ps laser processing were a subject of intense research. A very interesting approach developed for thin films on transparent substrates was the simultaneous use of front- and back-surface reflectivity measurements upon laser exposure, as shown in [57].

The use of point-probing measurements in the analysis of the dynamics of phase transitions associated to phase change optical recording materials [58, 59] has also been extremely successful. The use of real-time optical measurements provided an ideal alternative to differential scanning calorimetry, analyzing thermally induced phase transitions occurring in transformation windows from 1 to 10^4 μs over micron-size-irradiated regions, as first shown in [60]. The demonstration of ultrashort pulse-induced reversible phase transitions in phase change materials [61] evidenced the need of increasing the time resolution of “real-time” point-probe measurements to the sub-nanosecond regime not only in the case of phase change materials but also in rapid solidification phenomena induced with ps laser pulses [62]. This can be achieved by using single-shot streak cameras to detect sample reflectivity or transmission changes for bursts of ps-probe pulses closely spaced in time [63] or using a relatively long (~1 μs), single-mode, temporally square probe laser pulse to achieve a temporal resolution close to 10 ps [64]. This approach was also used to analyze ultrafast phase transitions in InP [65] but resulted especially useful to demonstrate for the first-time reversible (amorphization and crystallization) phase transitions in GeSb films irradiated with ps pulses occurring over a time window of less than 400 ps [66]. The same approach of optimizing latent heat release and heat flow in the thin film structure was later on used in GeSbTe films to demonstrate ps-laser pulse-driven, reversible phase-change optical recording and resolve the respective phase transformation times [67].

Although the above examples can be considered as “historical,” phase change materials, specially chalcogenides, are still very attractive for a wealth of applications, and real-time reflectivity measurements are still an essential tool for the investigation, for instance, of multilevel recording applications [68] or tunable

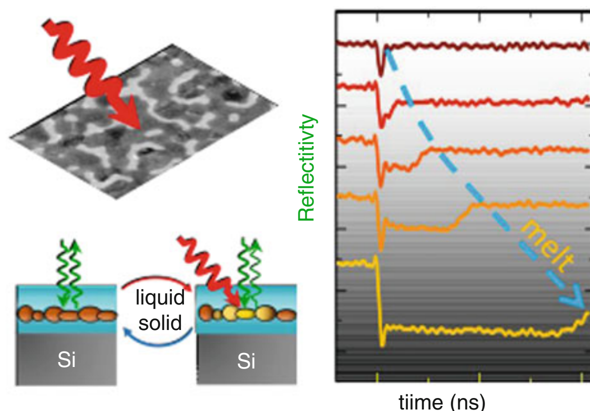

Fig. 7.5 Laser-induced transient phase change of an embedded single layer of near-coalescence Bi nanostructures (random metasurface) from solid to liquid and back to solid upon cooling. The ns pump pulse is indicated in red the cw probe beam in green. The graph displays real-time reflectivity measurements of the phase transitions at different pulse energies. The lower reflectivity is a signature of the molten phase. (Reprinted with permission from [71] © Wiley)

nanophotonics [69]. The same applies to other applications related to laser-induced phase transitions like the assessment of novel mechanisms in during the formation of the so-called laser-induced periodic surface structures (LIPSS, see also Chap. 23) in semiconductors [70] or the investigation of reversible laser-induced switching in random metasurfaces based on disordered bismuth nanostructures [71]. The latter study (c.f. Fig. 7.5) demonstrates how this technique is capable of quantifying the melt duration even for an ultrathin Bi nanoparticle layer (5 nm thick), demonstrating tunability over a range of 10–700 ns by changing the pump fluence. The pump laser-induced transient state of low reflectivity can be exploited for the fabrication of nanophotonic switching devices.

2.3 Ultrafast Point-Probing: From the Visible to the X-Ray Regime

Given the immense advances in ultrafast science over the last decades and the scope of the book, we will limit this section to review some time-resolved (pump-probe) optical techniques and experiments with fs-resolution in point-probing configuration, involving the interaction with condensed systems. We will therefore not comment on pump-probe experiments in the fields of femtochemistry [72], ultrahigh intensity interactions [73], attoscience [74, 75], and related fields. On the other hand, the availability of ultrafast image-based techniques [76, 77] (see Sect. 2.4) generated an essential step in our comprehension of ultrafast interactions in condensed systems, beyond the information derived from point-probing experiments.

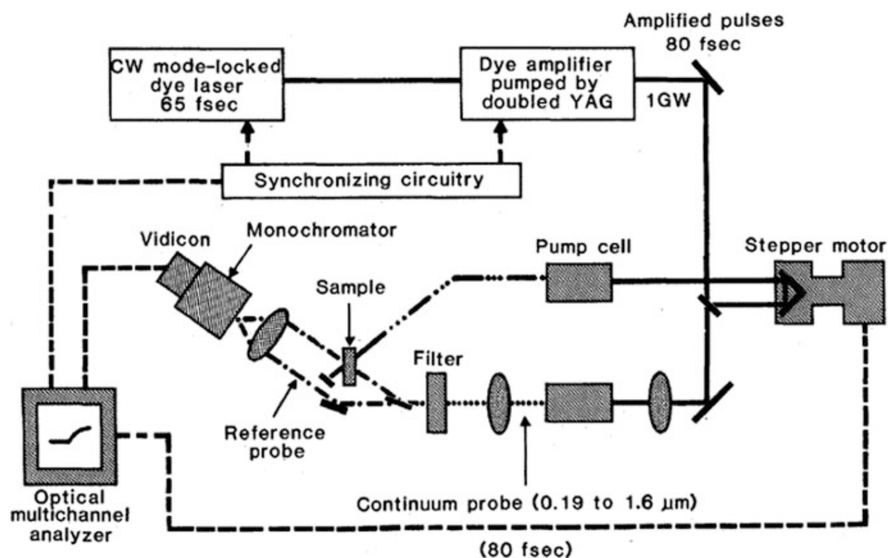

Fig. 7.6 Schematic of apparatus for femtosecond time-resolved spectroscopy according to the description in reference [79]. Notice the use of probe pulses extracted from a supercontinuum source

For what concerns the early use of optical point-probing measurements with ps- and fs-resolution, it is remarkable that already in the late seventies, a number of techniques based on this scheme were already well established and applied to the study of a variety dynamic processes [78]. In 1983, Charles Victor Shank from Bell Labs published a small review in Science entitled "Measurement of ultrafast phenomena in the femtosecond time domain" [79], where the expected developments of fs-resolution spectroscopy were envisaged. Optical reflectivity, transmission, and absorption point-probing measurements, using not only monochromatic sources but also white light continuum sources (see for instance [80]), were already available in 1983. Figure 7.6 shows a typical layout of a point-probing, pump-probe fs-resolution experiment. The amplified laser pulse is split in a lower- and higher-energy component that reaches the sample after passing through a variable delay line. The lower energy pulse interrogates the excited region (in this case its transmission relative to a reference probe) at a selected delay with respect to the pump pulse, enabling the reconstruction of the measured property evolution as a function of time.

When the process is reversible, it is possible to use a static sample, something not possible when analyzing phenomena involving structural transformations for which, during the experiment, a fresh region of the sample needs to be exposed for every measurement. The same year (1983), Shank and coworkers published two crucial papers for the comprehension of ultrafast laser-induced phase transitions in semiconductors. In one case they used multiple wavelengths from a white

light continuum source [81] to measure the reflectivity evolution of the fs-laser-irradiated surface; in the second case, they employed second-harmonic generation [82] as a point-like probes. Both papers proved by means of different methods the formation of a highly excited, disordered structural state of Si within a fraction of a picosecond upon excitation, followed by a transition to ordinary molten silicon in a few picoseconds. Figure 7.7 shows a polar plot of the second-harmonic intensity generated at the surface showing a strong decrease of the intensity (at $\varphi = 120°$) consistent with a strong perturbation of the ternary symmetry of the <111> Si surface within about 240 fs. The formation of an isotropic surface of molten Si is found to require a longer time, about 3 ps.

These two works were the first demonstration of the existence of a nonthermal ultrafast melting process in Si upon irradiation with sub-picosecond laser pulses. This phenomenon was later on observed in other semiconductors, like GaAs [83, 84], but also in other materials, like chalcogenide-based films for optical recording [85]. Related to this topic of ultrafast phase transitions, electronic excitation-enhanced crystallization in amorphous GeSb films excited with fs-laser pulses was demonstrated in 1996 [86].

Along with these two techniques (multi-wavelength reflectivity and second-harmonic point-probing), the development of other ultrafast point-probing techniques like time-resolved ellipsometry and dielectric function measurements enabled the access to a more detailed view of the evolution of the optical properties of the irradiated material. The first single wavelength ellipsometry measurements with ps resolution date from 1974 [87]. The extension to the fs-regime had to wait for nearly 20 years [Choo 1993]. This technique has recently been revisited to enable spectroscopic ellipsometry measurements with a resolution close to 100 fs over a spectral interval of 1.3–3.6 eV [88]. A direct measurement of the evolution of the dielectric function of materials with fs resolution upon irradiation was first reported in 1997 [89]. Figure 7.8 shows the setup as described in [90]. Reflectance is measured at two different angles over the white light continuum spectrum generated in a CaF_2 crystal. The measured values are used to determine the dielectric function by numerically inverting the Fresnel equations for reflectivity. This technique enabled to further confirm [77] the existence of electronic excitation-induced lattice disorder in GaAs [91] and was also used to analyze the presence of ultrafast phase transitions in GeSb films [92] upon fs laser excitation.

Although X-ray point probes are not strictly speaking "optical" probes, they have also been extremely successful in the analysis of structural transformation dynamics upon fs-laser excitation. In this respect, it is worth noting that there is only an indirect relationship between the optical and structural properties of crystals. This makes fs-resolved X-ray diffraction [93, 94] the only technique that may provide direct information about the structural dynamics, even at the nanoscale [95]. This topic is reviewed in detail along with other X-ray experiments in Chap. 6.

To conclude this subsection, it must be emphasized that optical point-probing, pump-probe experiments are also a useful tool for the time-resolved analysis of carrier and structural transformation dynamics in reversible structural changes. They have been thoroughly used, for instance, in highly correlated materials [96] and also

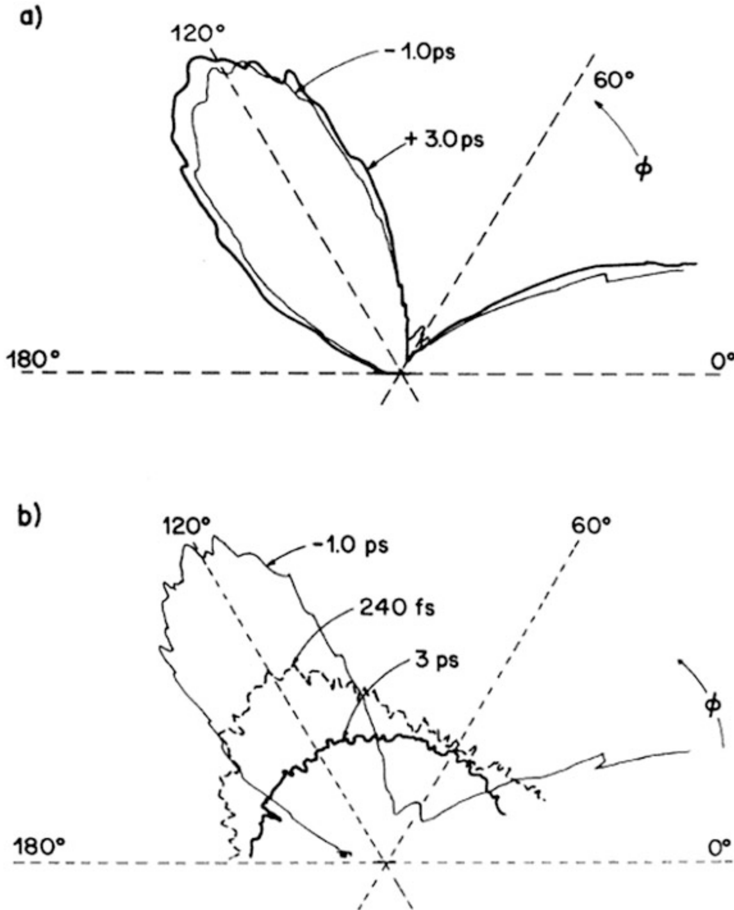

Fig. 7.7 (**a**) Polar plot of the second-harmonic intensity in Si as a function of time and angle (φ) for low pump energy, 0.5 E_{th}. (**b**) Polar plot of the second-harmonic intensity as a function of time and angle (φ) for pump energy 2.0 E_{th}. E_{th} is the surface amorphization threshold of Si at 620 nm (90 fs pulse duration). (Reprinted with permission from [82] © (1983) by the American Physical Society)

(beyond the optical regime) in THz spectroscopy [97] for the analysis of carrier dynamics in photovoltaics [98]. A particularly relevant application in the study of ultrafast dynamics has been their use for the study of coherent optical phonons (COPs). Optical phonons are called coherent when the oscillation phase is kept constant in a time range longer than the vibration period. An ultrashort laser pulse can excite coherent optical phonons through the sudden modification in free-carrier density and electron temperature, which perturbs the interatomic potential. This results in a displacement of the atoms, acting like an external force on the vibrational degrees of freedom [99]. Since COPs occur on an atomic-scale, X-rays are the

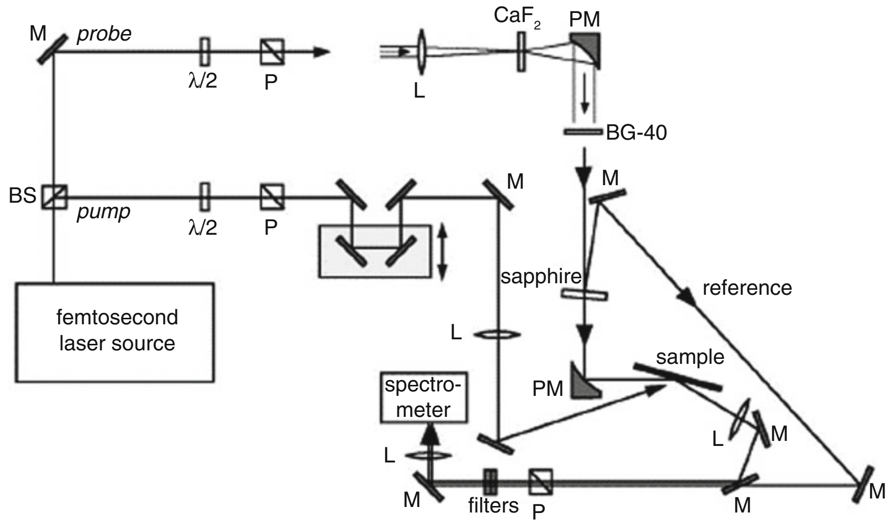

Fig. 7.8 Scheme of the setup for time-resolved dielectric function measurements by dual-angle reflectometry. BS polarizing beam splitter; M flat mirror; PM parabolic mirror; L lens; P polarizer; and λ/2 half-wave plate. (Reprinted from [90] with the permission of AIP Publishing)

ideal tool to follow the related lattice dynamics [100]. However, optical probes may be used to detect and analyze coherent optical phonons due to the changes in reflectivity associated to Raman active vibrations. This feature has been used to analyze coherent phonon dynamics in a variety of systems including, among others, phase change materials [101] in amorphous and crystalline phase [102].

2.4 *Ultrafast Surface Microscopy*

In 1985, M.C. Downer, R.L. Fork, and C.V. Shank introduced a novel technique, combining a pump-probe approach with optical microscopy [76, 103]. This new experimental system was presented as the natural evolution of the previous work of C.V. Shank et al. [81], in which point-probing reflectance was monitored with a photodiode. The interest of this technique lies in two main aspects. First, it provides direct images of the surface, which makes the qualitative analysis of the transformation dynamics simpler than in other techniques. Second, it gives simultaneously access to the reflectivity evolution of the material both in time, *t*, and space, *r*. That way, the material response at different local fluences is obtained since the beam profile normally shows a spatial Gaussian distribution. Figure 7.9a shows a set of recorded images upon excitation of crystalline silicon with an 80 fs pulse at 620 nm.

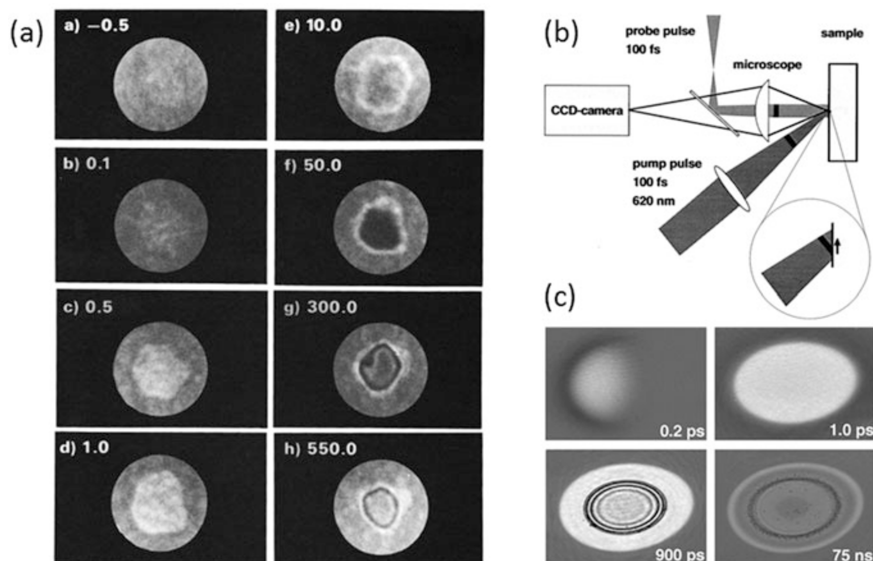

Fig. 7.9 (**a**) Images of the evolution of the surface reflectivity of a silicon sample after irradiation. The numbers in each image correspond to the temporal delay (in picoseconds) after excitation. (Reprinted with permission from [103] © Springer). (**b**) Sketch of time-resolved microscopy. In this particular case, the pump pulse reaches the sample at an oblique angle and the probe pulse normal to the surface. (Reprinted with permission from [104] © Elsevier). (**c**) Time-resolved images (time delay labelled on each image) of the surface of a silicon wafer after irradiation. Frame size 220 μm × 300 μm. (Reprinted with permission from [105] © (1998) by the American Physical Society)

A step forward in the development of this technique was made in 1997 by D. von der Linde, K. Sokolowski-Tinten, and coworkers [105, 106], by capturing the evolution of the reflectivity with a CCD camera instead of photographic paper, while reversing the angle of incidence of the pump and probe beam. The experimental setup is sketched in Fig. 7.9b. This technique resulted in high-quality digital images, as shown in the Fig. 7.9c for a silicon sample, which allowed better quantitative analysis by digital processing. As a first example of the high-spatial and temporal resolution, the image recorded at a delay 0.2 ps resolves the *landing* of the pump pulse (incident from the left). Since the incidence angle of the pump beam was 45°, the left part of the image first experiences a change of reflectivity triggered by the generation of free electrons. From the Fresnel equation and Lorentz-Drude modelling, it is possible to estimate the temporal evolution of free electron density. A second example, demonstrating the huge potential of this technique to unravel ultrafast laser-matter interaction mechanisms, is the observation of transient Newton rings at delays on a scale of hundreds of picoseconds (900 ps in the image of Fig. 7.9c). The rings are formed by constructive and destructive interference of the probe light partially reflected at the top and bottom interface of an expanding layer

of ablated material. The analysis of the number of rings at different time delays allowed to measure the expansion velocity of the ablating layer (~1000 km/h) and enabled to assess the thermodynamical mechanisms responsible for the ablation process (isochoric heating, adiabatic expansion, rarefaction wave propagation, phase explosion) [104].

Beyond the study of electronic excitation-induced disorder (nonthermal melting) [77, 107, 108], time-resolved microscopy has mainly focused on the study of the ablation dynamics of materials, which, as indicated above, is a process where matter is subjected to extreme thermodynamic conditions. In the case of dielectrics, fs-resolved microscopy has the additional advantage of facilitating the analysis of nonlinear absorption mechanisms. Several research groups have investigated the ablation dynamics of dielectrics, including the fs-resolved microscopy studies in sapphire, fused silica, quartz, or lithium niobate among others by authors of this chapter [109–111]. Figure 7.10a shows three snapshots of a fused silica surface recorded at different time delays after irradiation, together with the temporal evolution of the reflectivity at different positions (local fluences). At ultrashort time delays, a strong transient increase in surface reflectivity (up to five times) is observed, reaching its maximum at several some 100 s of femtoseconds after the arrival of the pump pulse. This delay in the occurrence of the reflectivity maximum implies a delay in reaching the maximum free electron density after pulse absorption, stressing the important role of impact ionization in the carrier excitation process. Further studies in dielectrics allowed to observe the formation of transient Newton rings also in other dielectrics [112], as shown in Fig. 7.10b. This observation indicates that some of the main physical mechanisms underlying ultrafast ablation are material independent.

This technique has also been used to characterize the temporal dynamics of other types of material transformations, for instance, for the case of crystalline silicon with a micrometric dielectric sphere placed on the surface (c.f. Fig. 7.10c). This experiment allowed to characterize the effect of strong local field enhancement (near field) on laser material processing [113], an effect that is discussed in more detail in Chaps. 8 and 11. Another example is illustrated in Fig. 7.10d, showing time-resolved images that reveal the formation dynamics of a thin heat-affected layer at the surface of phosphate glass. This sub-ablative effect, as demonstrated by the laser-induced surface elevation in AFM image (instead of depression), is quantified via image analysis (contrast and number of Newton's rings) and optical modelling. It should be noted that the time window to observe this effect lies in the 100 s of nanosecond's range after irradiation, which required the implementation of a long optical delay line, implemented by means of optical fibers for the probe beam [114]. Finally, Fig. 7.10e shows transient reflectivity images of the material transformation pathway, leading to the formation of laser-induced periodic surface structures (LIPSS) on silicon. It has to be emphasized that these structures are formed by the effect of multiple pulse irradiation. The experiment, using a special layout ("moving spot") enabled to demonstrate that the LIPSS formation process in this case is initiated by free electron generation leading to nonthermal melting, liquid phase overheating, and rapid solidification into the amorphous phase [115].

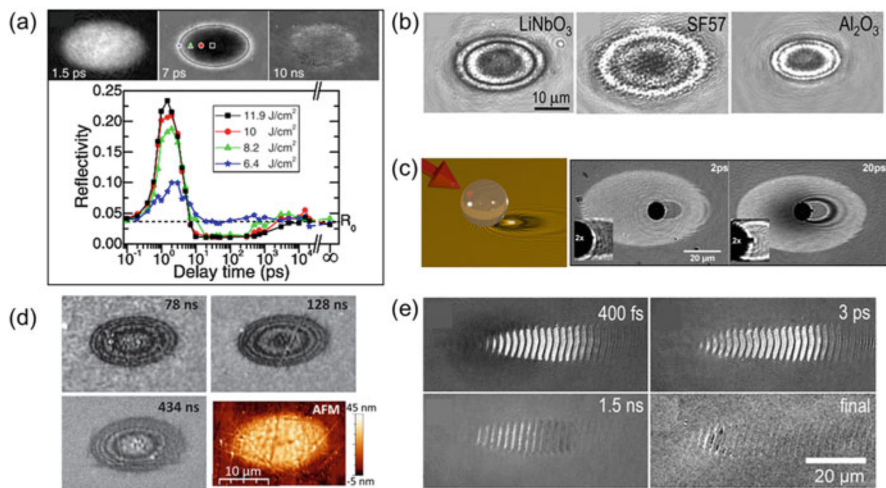

Fig. 7.10 (**a**) Time-resolved reflectivity images and their temporal evolution upon single pulse fs laser excitation of fused silica. The analysis is performed at different radial positions, corresponding to local fluences that range from close to the ablation threshold (blue stars) to well above (black squares). (Reprinted with permission from [109] © The Optical Society). (**b**) Time-resolved reflectivity images of laser-irradiated dielectrics recorded with sub-nanosecond time delays ($LiNbO_3$ at 315 ps, SF57 glass at 415 ps, and Al_2O_3 (sapphire) at 215 ps), featuring transient Newton's rings. (Reprinted from [112] with the permission of AIP Publishing). (**c**) Left. Schematic view of the spatial intensity distribution in the vicinity of a micrometric spherical particle irradiated by the laser at oblique angle. Right. Surface reflectivity images at the particle location for two different delays (indicated). Image from [113]. (**d**) Time-resolved reflectivity images at different time delays after irradiation of a phosphate glass with fluences below the ablation threshold. The bottom right frame shows an atomic force microscope (AFM) image of the permanent surface modification induced. (Adapted from [114] with permission from the authors). (**e**) In-situ microscopy images of the silicon surface recorded at different delay times during laser writing of self-organized amorphous fringes (LIPSS). (Reprinted with permission from [115] © 2016 American Chemical Society)

Before describing more complex ultrafast time-resolved imaging techniques, we will briefly revise some other recent results derived from time-resolved microscopy experiments. Winkler and co-workers [116] observed and characterized laser amplification in excited dielectrics. In a pump-probe experimental configuration in which the sample surface was imaged from the backside, it was observed that the probe beam was coherently amplified while propagating inside an excited dielectric. This amplification starts to increase around 100 to 200 fs after excitation and is sustained for several tens of picoseconds in a thin sapphire sample. Pan and coworkers [117], using a setup similar to the one sketched in Fig. 7.10c, have recently studied the transformation dynamics of molybdenum disulfide, a semiconductor material attracting considerable interest because of its potential applications in optoelectronics. More recently, Xie and coworkers [118] have used time-resolved microscopy to characterize a pump-induced transient micro-grating generated by

the Kerr effect. This strategy is proposed as a solution for the determination of an absolute pump-probe delay and pulse-front tilt detection.

Although time-resolved microscopy has been demonstrated to be a very powerful technique, the obtained information corresponds to changes in the amplitude of the illumination beam (reflection or transmission) alone. In order to access other optical parameters (polarization or phase with spectral resolution), it is necessary to use alternative approaches. Different experimental strategies, combining the use of time-resolved microscopy with the determination of additional parameters, have been developed. The most relevant ones can be grouped into time-resolved ellipsometry and time-resolved interferometry experiments, as described in more detail in the following sections, together with time-resolved imaging of non-specular scattered light with is described in detail in Chap. 9.

Ellipsometry encompasses techniques that analyze the intensity and state of polarization of a light beam after it has been reflected off a surface, allowing access to the dielectric function of the material under study. Wang and Downer [119] carried out the first work on single-wavelength ellipsometry with temporal resolution upon material excitation with fs laser pulses. More recently, different groups have proposed the combination of ellipsometry and time-resolved microscopy, the so-called ultrafast pump-probe imaging ellipsometry [120–122]. In this particular case, the approach is based on the use of a single wavelength and different incidence angles. The procedure consists in recording a set of images for each time delay, polarizer and analyzer settings for different angles. By analyzing the reflectivity of the images at different angles, local ellipsometry measurements as a function of time are obtained. From these data, and the application of Fresnel equations, the components of the time-dependent complex refractive index can be retrieved. This technique is especially useful for characterizing events occurring in the timescale up to 10s of picoseconds after irradiation, where the images recorded with the conventional time-resolved microscopy are usually dark, either due to interferential effects (destructive interference) or absorptive process. The determination of the transient complex refractive index allows to extract the optical penetration depth and assess the roles of absorption and interference in the observed behavior.

Another alternative to determine the dielectric function (spectroscopic approach) has recently been proposed in [123]. In this case, the s and p components of the polarization of the probe beam at different delays and as a function of the probe wavelength are measured. The experimental setup is shown in Fig. 7.11a along with an inset showing two example images. The temporal evolution of the reflectivity intensity for each of the polarization components is plotted in Fig. 7.11b for each probe wavelength. The results extracted from this analysis allowed to discover a possible additional absorption channel for p-polarized light.

In the above description, the shown techniques are based on directly recording the reflected or transmitted light from an illuminated surface (area), allowing to access the amplitude or polarization of the electric field. Another relevant property of the field is the phase, which can be retrieved by interferometric techniques. In the following paragraphs, three different approaches for time-resolved interferometry will be revisited. In the first one, an evolution of conventional fs-resolved

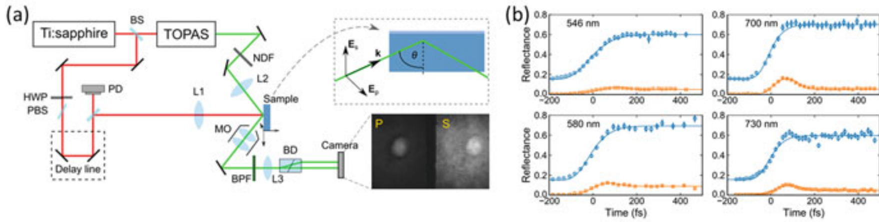

Fig. 7.11 (**a**) Pump-probe setup for measuring simultaneously s- and p-polarized reflectance. The probe wavelength is tunable by making use of an opto-parametric amplifier. Before the CCD, a beam displacer (BD) separates the reflected s and p components, being recorded simultaneously. (**b**) Time-dependent s- and p-reflectance data (blue circles and orange squares, respectively) at different probe wavelengths. (Adapted with permission from [123] © (2020) by the American Physical Society)

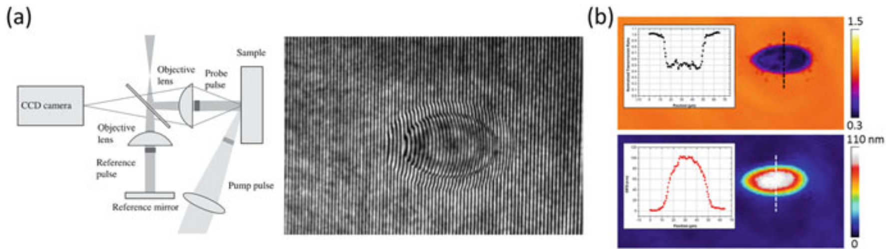

Fig. 7.12 (**a**) Left. Setup for ultrafast interferometry with imaging configuration. Right. Transient interferometric image of an ablating GaAs <100> surface excited with $F = 1.4$ F_{abl}, recorded at a temporal delay of 1.4 ns. Reprinted with permission from [124] © Springer. (**b**) Example of the spatial information on transmission and optical path difference (OPD) extracted after recording with a wavefront sensor the probe beam transmitted through an excited Nb_2O_5 film (delay of 18 picoseconds). (Adapted from conference presentation by authors of ref. [126], available at https://www.fresnel.fr/perso/gallais/)

microscopy incorporating a Michelson interferometer [124, 125] was developed. The corresponding setup is shown in Fig. 7.12a. On the right side of the same figure, an image of the recorded interference pattern for a delay of 1.4 ns after irradiation of GaAs with a single femtosecond pulse is shown. From these images and their analysis, it is possible to distinguish phase contributions induced by changes in the optical constants and surface deformation.

A different strategy was followed in [127], where the intensity and phase of the probe beam after interacting with the excited material is recorded with a 2D-wavefront sensor instead of a regular CCD. After mathematical processing, these two quantities can be separated into two different images, one accounting for the absorption (top image in Fig. 7.12b) and one representing the optical path difference (OPD) (bottom image in Fig. 7.12b).

The two techniques described above correspond to interferometry measurements in the space domain. A different approach is frequency-domain interferometry,

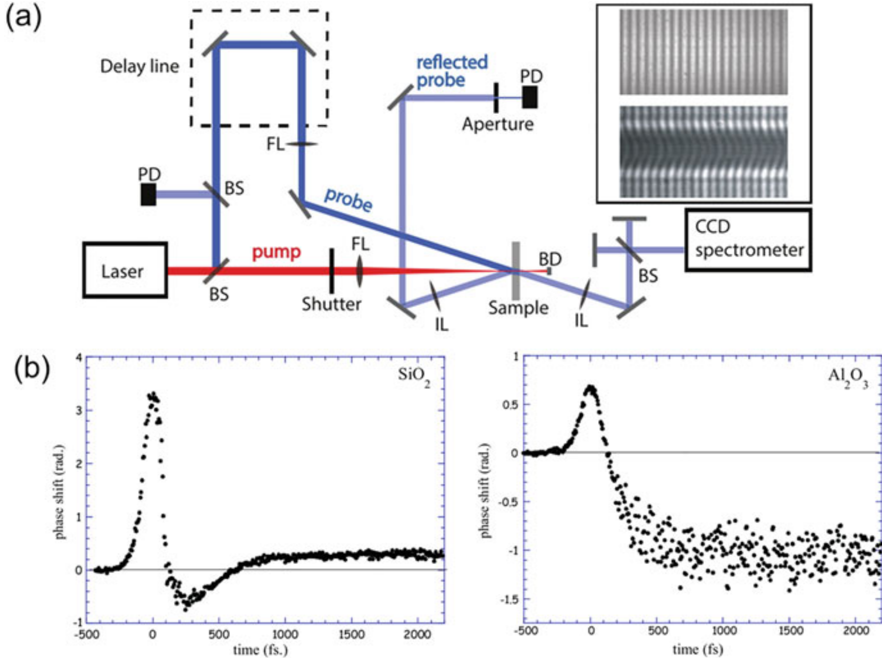

Fig. 7.13 (**a**) Schematic of a time-resolved interferometry setup. BS beam splitter. FL focusing lens. IL imaging lens. PD photodiode. BD beam dump. The inset shows two examples of CCD images recorded with (bottom) and without (top) laser excitation. (Reprinted with permission from [130] © IOP Publishing) (**b**) Temporal evolution of the measured phase shift in fused silica (SiO_2) and sapphire (Al_2O_3). The pump irradiation intensities are well below the ablation threshold fluence. (Reprinted with permission from [131] © Springer-Nature)

as first reported in this field by Audebert and coworkers [128, 129] and further exploited and improved by the group of Guizard [130, 131]. As shown in Fig. 7.13a, the experimental setup includes an interferometer and a spectrograph with a CCD. The Michelson interferometer is located behind the sample and splits the probe beam in two parts. The interferometer is slightly misaligned, projecting onto the spectrograph slit the two beams laterally displaced. This causes that one beam to act as a probe beam, carrying information of the excited region, and the other as a reference beam, carrying information of the non-excited region. Both beams enter the spectrograph, and the spectral interference pattern is imaged onto a CCD. Figure 7.13a also includes two examples of interference images recorded with the CCD, situated at the spectrograph output. The upper image shows a featureless interference pattern, corresponding to a situation of negative time delay (probe beam arrives earlier). In contrast, the lower image corresponds to a situation after excitation, leading to a strong distortion (phase shift) and change of intensity (absorption) in the fringes.

Figure 7.13b shows a plot of the phase shift evolution as a function of time for two different materials: fused silica (SiO_2) and sapphire (Al_2O_3). The phase shift is directly related to the change of the real part of the refractive index [131]. At ultrashort time delays, a positive phase shift is attributed to the nonlinear optical behavior of bound electrons (nonlinear Kerr effect), caused by the presence of the intense excitation beam. This effect is observed in both materials (see Fig. 7.13b). The observation of the Kerr effect allows to precisely determine the arrival time of the pump pulse to the sample surface. Immediately afterward, a negative contribution to the refractive index that leads to a negative phase shift is caused by the photo-generated electrons (N_e), as already described in the Drude-Lorentz model. This decrease of the phase shift due to the generation of free electrons is observed after the Kerr effect in both materials. Finally, a recovery of the phase shift to positive values is observed for fused silica, as opposed to the case of sapphire. The recovery in silica is due to the formation of self-trapped excitons (STE), which contributes to an increase of the refractive index.

When used in transmission, frequency domain interferometry also provides information about the absorption experienced by probe beam, thus giving access to the imaginary part of the refractive index. However, this approach has two main disadvantages. First, only transparent materials or very thin films on transparent substrates can be studied. Second, the sampling beam does not only probe the surface (where the energy deposition is highest) but also probes laser-induced changes occurring in deeper regions, effectively providing and average measurement over the interaction depth. This problem, and the related ambiguities, can be sorted out combining in the same setup femtosecond-resolved microscopy and frequency-domain interferometry, as reported in [11].

2.5 Ultrafast Shadowgraphy

The most basic configuration of ultrafast shadowgraphy is actually very similar to the transmission probing configuration of laser-induced surface changes presented in Sect. 2.4. A typical ultrafast surface microscopy configuration that can be rapidly switched between reflectivity and transmission modes has been reported in [132], based on a probing incidence either from the front side or the back side of the sample. Yet, most ultrafast shadowgraphy studies employ a configuration in which the pump beam and the probe beam enclose an angle of 90°, which corresponds to a side view of a laser-matter interaction region. With this configuration, a variety of different mechanisms can be investigated, of which the most frequent ones are summarized in the following subsections:

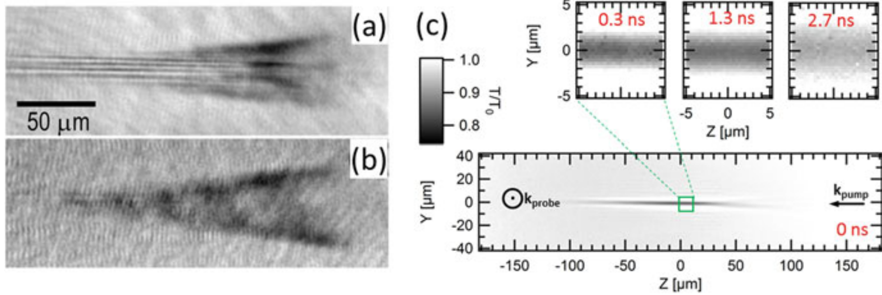

Fig. 7.14 (**a**, **b**) Shadowgraphs recorded inside phosphate glass upon irradiation with single pump laser pulses ($\lambda = 800$ nm). (**a**) corresponds to a pulse duration of $\tau = 100$ fs, whereas (**b**) to $\tau = 270$ fs. The pump pulse propagates from left to right the 400 nm; $\tau = 100$ fs probe pulse is incident from behind. Reprinted from [133] with the permission of AIP Publishing. (**c**) Shadowgraphs recorded in bulk silicon after the irradiation with a single pulse ($\lambda = 1300$ nm, $\tau = 90$ fs). For increasing time delays (bottom part), diffusion of free electrons is observed. The laser pulse propagates from right to left. (Provided by the authors of [136])

2.5.1 Electron Plasma Formation Dynamics Inside Materials

Employing ultrafast shadowgraphy, numerous groups have investigated the plasma formation and relaxation dynamics of laser-excited regions inside a material. One example can be found in [133], in which the technique was applied to investigate nonlinear propagation, excitation, and modification inside phosphate glass. In this study, a train of fs laser pulses was focused 1.56 mm below the surface while transversally displacing the sample, which led to the inscription of optical waveguides. Figure 7.14a, b display shadowgraphs of individual pulse recorded at different time delays, visualizing regions where free electrons are generated (dark regions) during pump pulse propagation. The corresponding electron density can be estimated by means of quantifying the local absorption and applying a simple Drude model. Moreover, in (a) the presence of pronounced beam filamentation can be appreciated, as well as the distorsion of the focal volume (expected to be of elliptical rather than arrow head shape). Filamentation can be avoided by a slightly increasing the pulse duration, as demonstrated in (b). Focal volume distortion, caused by pre-focal depletion, is more difficult to prevent but can be minimized by a reduction of pulse energy and multiple overwriting at lower energies. Both strategies were shown to greatly improve waveguide performance [133]. Other groups have investigated by means of shadowgraphy filamentation behavior and electron dynamics in more complex situations, such as double pulses and multiple pulses [134].

An interesting modality of the basic shadowgraphy setup has been introduced by Sun et al. [135]. By means of dividing the probe beam after the sample in two, and spatially overlapping the probed region with a non-probed region on the CCD camera (similar to the technique introduced in Sect. 2.5 [11]), additional information can be extracted. In particular, the transient change of the real part of the refractive

index as well as the electron-electron collision time for a given pump energy can be extracted. Alternatively, phase contrast microscopy also provides access to the time-resolved changes of the refractive index [136].

Even more challenging is the investigation of these processes in semiconductors that are nontransparent to visible light. Pioneering work in this field has been performed by the group of Grojo, applying femtosecond-resolved shadowgraphy to the study of fs excitation inside bulk silicon [137]. This study required the use of pump and probe wavelengths in the spectral range where silicon becomes transparent ($\lambda > 1100$ nm), as well as the use of cameras with infrared sensitivity. Figure 7.14c displays typical time-resolved shadowgraphs, revealing that the laser-excited electron plasma is very elongated, in part due to the strong refraction of silicon, increasing significantly its width at longer delays, which is indicative of radial electron diffusion.

2.5.2 Surface Ablation and Shockwave Expansion

Besides exploiting shadowgraphy for resolving ultrafast plasma formation and relaxation dynamics, the technique has been widely applied to the study of a number of other processes. In particular, surface ablation and the accompanying shockwaves expanding in the surrounding air, as well as stress waves inside the material, have been the focus of interest since long. While the shock waves can also be studied to some extend with ultrafast surface microscopy (see Sect. 2.4), the information obtained is rather limited. Ultrafast shadowgraphy has the advantage of providing a side view of the expanding wave and thus directly yielding quantitative information about the axial expansion velocities. An example can be seen in Fig. 7.15a–d, showing different stages of the expansion of a shockwave in air, accompanied by a stress front propagating into the material along the direction of the long-lived filament, formed at an early stage [138].

Although so far rarely used for the study of ultrafast laser-induced processes, the work of the Vogel group should be included in this section. They developed advanced microscopy techniques for shadowgraphy. Figure 7.15e–g displays shadowgraphs recorded with different modalities, clearly demonstrating the enormous contrast enhancement and revealing features that are not seen with standard shadowgraphy [139].

2.6 Ultrafast Continuous Imaging (UCI) Techniques

The previously discussed time-resolved techniques can be grouped in those offering the complete temporal evolution for a single-laser excitation event (Sect. 2.2) and those that record only one time-gated signal at a given delay value per laser pulse (Sects. 2.1, 2.3, 2.4, and 2.5). The latter requires therefore exposure to many laser pulses at different pump-probe delays in order to reconstruct the complete temporal

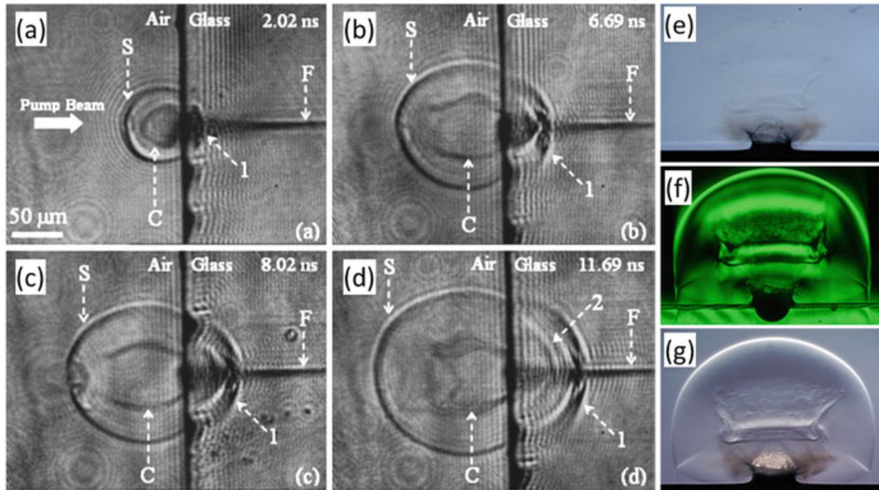

Fig. 7.15 (**a–d**) Shadowgraphs recorded at an air/silica interface upon irradiation with a single pump laser pulse ($\lambda = 800$ nm, $\tau = 100$ fs) at $F = 40$ J/cm^2. S shockwave front; C contact front; 1: first stress wave front; 2: second stress wave front; F filament. Reprinted from [138] with the permission of AIP Publishing [138]. (**e–g**) Shadowgraphs recorded at the air/water interface upon irradiation with a single pump laser pulse ($\lambda = 2940$ nm, $\tau = 80$ ns, $F = 5.4$ J/cm^2) from the top, recorded at a delay of 2300 ns. The different appearance is caused by the different imaging modalities used. (**e**) Bright-field shadowgraphy. (**f**) Dark-field shadowgraphy. (**g**) Combined Hoffmann modulation shadowgraphy combined with a knife-edge technique. (Provided by author of ref. [139])

evolution. Time-gated techniques offer a far superior temporal resolution than real-time techniques, but the inherent need for multiple laser exposure can be a serious limitation. While single-pulse-induced dynamics can in principle be investigated with time-gated techniques by exciting a previously unexposed region for each delay time, this method requires the absence of significant pump pulse fluctuations and a spatially homogeneous sample, which is sufficiently large for exposure to numerous (typically $N = 20$–100) spatially separated laser excitation spots (typical diameter $d = 20$–100 µm, separation $s = 2{*}d$). Yet this requirement to the sample cannot always be met. In particular, this is an issue for samples that are not sufficiently homogeneous (e.g., often the case for thin films grown by certain techniques in research labs), costly to be fabricated in such a size (e.g., samples produced by electron/ion beam lithography), inherently inhomogeneous samples (e.g., biological samples), or evolving samples (e.g., living tissue, chemical reactions).

Motivated by this need for high temporal resolution techniques with true single pulse measurement capability, a range of advanced techniques has recently been developed, often termed as continuous optical imaging techniques. The basic concept that most of them share is the use of a single excitation pulse to induce the transformation, combined with multiple probe pulses arriving at different time delays, which can be distinguished and separated by their individual spatial

positions, angles, wavelengths, states of polarization, or spatial frequencies. An exception is a technique that does not require probe pulses but relies on the detection of luminescence or scattered pump light [140], explained in more detail at the end of this section.

In the following, we summarize them and briefly explain the basic measurement principles. A more detailed overview can be found in the excellent reviews of Guo et al. [141, 142], Liang et al. [143], and Mikami et al. [144]. There are undoubtedly other powerful techniques in this very active field of research that do not fall in this categorization and which we left out here in order to not exceed the length of this section.

2.6.1 Spatial Division UCI

In the pioneering work of the Nelson group [145], a true single pulse point-probing technique was introduced. By means of introducing two specially designed optical components in the probe beam path, sketched in Fig. 7.16a, the so-called echelons, the large-diameter probe beam, could be subdivided into 20×20 sub-beams, each with a different optical delay with respect to the pump pulse. After probing the sample, the beam was sent to a CCD camera for recording. The technique also includes an elegant method for normalizing the spatial intensity inhomogeneities of the probe beam, by generating a reference image of a fraction of the sub-divided beam that had not probed the sample, and which is simultaneously recorded by the CCD camera. The echelons were designed to yield a delay step size of 25 fs, and the useful delay window achieved was 10 ps. The results obtained in their study of chemical reactions allowed a single pulse real-time transmission measurement with high temporal resolution and extremely low noise (as low as 0.1% of the transmitted probe light intensity) [145].

A straight-forward further development of this technique, coined multiframe femtosecond time-resolved optical polarography (M-FTOP), was reported by Wang et al. [147]. The authors traded the high-single-pulse sampling capability for gaining 2D spatial resolution by using a single echelon only, which allowed the 2D imaging of an fs laser beam propagating in a transparent material (c.f. Fig. 7.16c). Since the echelon generated a spatially dependent probe pulse arrival at the propagation/imaging plane, snapshots at different delay times, spaced by 0.96 ps, could be recorded with a single camera upon single-pulse irradiation, as shown in Fig. 7.16d. It should be noted that it is the Kerr effect that causes the propagating pulse to be visible to the recording CCD, inducing a transient birefringence in the material, which is detected by introducing crossed polarizers in the setup.

2.6.2 Temporal Wavelength Division UCI

One of the drawbacks of the space division–based methods described in the previous section is the use of a physical echelon, which leads to a fixed delay between probe

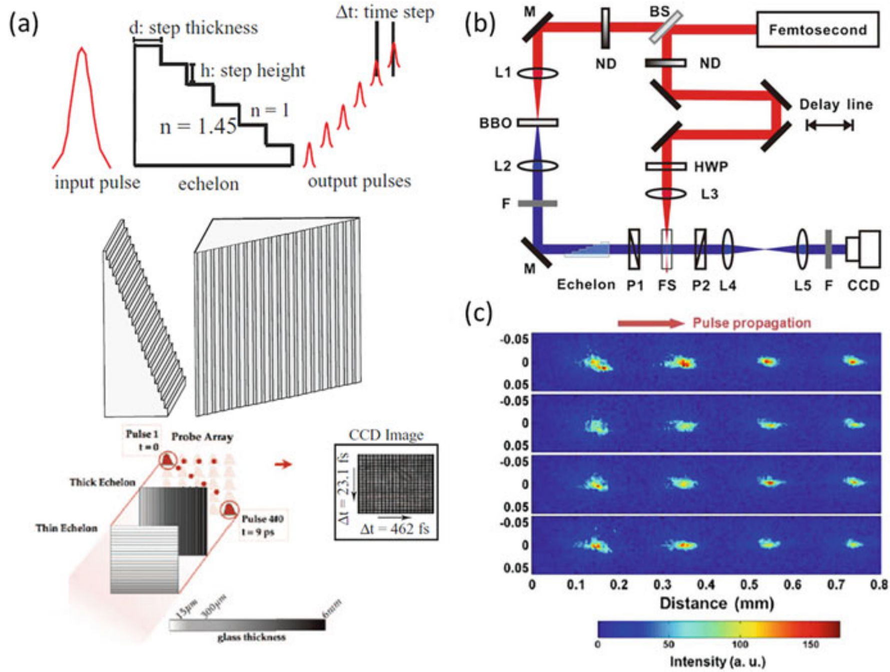

Fig. 7.16 UCI techniques based on spatial division and representative results. (**a**) Concept of the technique reported in [145, 146]. Reprinted with permission from [146] © AIP Publishing. (**b**) Sketch of the technique reported in [147] and (**c**) results obtained. Each row corresponds to the data obtained in a single pulse experiment. The different rows show data taken under the same conditions and the differences seen are caused by pulse fluctuations, underling the importance of UCI techniques. (Reprinted with permission from [147] © The Optical Society)

pulses that depends on the design of the echelon. A powerful technique reported in 2014 that allows a dynamical tuning of the interpulse delay is the so-called sequentially timed all-optical mapping photography (STAMP) [148]. Considerably more complex, the technique can be divided in three main steps required to prepare a suitable probe pulse train, as sketched in Fig. 7.17. In the first step, a single ultrashort probe pulse is stretched by means of introducing spectral chirp to a length that covers the desired temporal window of the process studied. To this end, the use of a glass rod allows stretching within the fs domain, whereas the use of a prism pair gives access to a ps temporal window, and the propagation of the pulse in a long fiber offers access to an ns temporal window. The second step consists in splitting this continuous chirped pulse into individual daughter pulses with a user-defined temporal spacing, employing a temporal pulse shaper based on a grating pair, a spatial light modulator and a 4-f imaging system. As a consequence of the initial spectral chirped pulse, the different pulse segments have different wavelengths (within the spectral bandwidth of the original ultrashort pulse). The third step, employed after probing the dynamics of the material, exploits

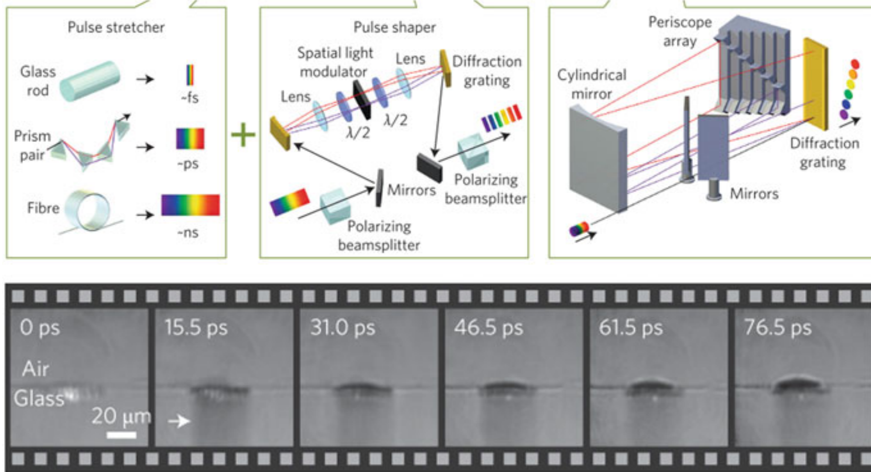

Fig. 7.17 UCI technique STAMP based on temporal division and representative results. Top row: Different steps of modifications applied to the probe pulse (left) pulse stretcher (middle) pulse shaper to generate daughter pulses (right) spatial mapping device, placed after probing the sample. Bottom row: Results of an ablation study in glass, showing the generation of a plasma filament and the generation and expansion of a plume caused by laser irradiation. (Reprinted from [148] by permission from Springer-Nature)

this wavelength difference of the pulse segments by introducing a diffraction grating to diffract them at different angles in the horizontal plane. Afterward, the pulses multi-pass through an optical system based on a cylindrical mirror and periscope array, whose function is to separate the image-encoded daughter pulses with high spectral resolution without image distortion and optical loss, displacing them in the vertical direction and eventually reaching the CCD sensor to record a single multiframe image.

This technique has been applied to the study of several laser-matter interaction mechanisms, including the surface ablation on a glass substrate as shown in Fig. 7.17, as well as the high temporal resolution visualization of lattice vibrational waves in $LiNbO_3$ [148]. Since then, several modalities of this technique, such as spatially filtered STAMP [149], have been developed and applied to capture, for instance, the dynamics of the crystalline-to-amorphous phase transition of $Ge_2Sb_2Te_5$. A recent directly related technique, also based on temporally stretching the probe pulse and using different spectral bands that are temporally separated, is “Framing imaging based on non-collinear optical parametric amplification (FINCOPA)” [150]. The technique also employs step 1 of the STAMP technique but avoids step 2 (generating separated daughter pulses with a pulse shaper) through optical parametric amplification of different spectral bands of the probe pulse (after passing the sample) with a pump pulse to generate a time-gated image. The drawback of this technique is the experimental complexity and the need for multiple CCD cameras.

2.6.3 Angle Division UCI

UCI methods based on angle division rely on the acquisition of interferometric images captured simultaneously at different angles with a single CCD camera. One example is the so-called all-optical coaxial frame imaging (OCFI), in which a train of probe pulses coaxially illuminates the target and generates multiple holograms via interference with multiple reference pulses, individually delayed to span the time window of interest [151]. The authors demonstrate the potential of this technique by recording multiple time-gated images of different single pulse laser-matter interaction processes, such as surface ablation in aluminum foil and ionization in air. The advantage of this holography based technique, related to the non-UCI spectral imaging interferometry technique described in Sect. 2.4 [11], is the direct access to the phase, which allows a measurement of the real part of the refractive index.

Another angle division UCI technique is "single-shot frequency-domain tomography (SFDT)" [152]. Here, five probe pulses with different projection angles are overlapped both spatially and temporally at the target for continuous imaging of a transient, which was measured using spectral imaging interferometry. Applied to the study of laser pulse propagation in fused silica, the technique is able to record movies of the diffraction, self-focusing and filamentation via reconstruction by inverse-Fourier-transform of the hologram area associated with each probe pulse, and applying a tomographic image reconstruction algorithm.

2.6.4 Spatial Frequency Division UCI

The principle underlying spatial frequency division is the encoding of unique periodic modulations (spatial frequencies) in the beam profiles of each probe pulse in order to be able them. One such technique, "femtosecond videography for atomic and molecular dynamics (FRAME)" [153], employs this concept in a very similar way as done in structured illumination microscopy, where it is used for eliminating out-of-focus light [154, 155]. In FRAME, multiple probe pulses with the user-desired temporal separation are generated with a beam splitter configuration. Introducing ronchi (bar) gratings with different rotation positions in each arm, each probe pulse is encoded with its own fringe pattern with a unique orientation. This strategy allows detection of all probe pulses with a single camera since the individual images can be extracted via Fourier transformation and filtering.

Another UCI technique based on spatial frequency division is "time-resolved holographic polarization microscopy (THPM)," which can image the amplitude and phase distributions of two orthogonal polarization states of an ultrafast event [156].

2.6.5 Receive-Only (Passive) UCI

In contrast to the previously listed concepts of UCI, based on different encoding and reading strategies of a probe pulse train, other methods have been reported that rely on the detection of luminescence or scattered pump light using a detector with high temporal resolution, not requiring the use of probe pulses (receive-only, passive). An excellent review on these techniques can be found in [143]. Among them, one of the pioneering techniques in this field has been developed by Gao and co-workers [140], termed compressed ultrafast photography (CUP), which employs a digital micro-mirror device for spatial encoding and a streak camera for adding temporal resolution. The input image of an ultrafast moving object is encoded with a pseudo-random binary pattern and then temporally dispersed along a spatial axis using a streak camera with an open slit, equivalent to a temporal shearing operation. By applying a CUP reconstruction algorithm, the encoded spatio-temporal images recorded by the streak camera can be transformed into a time sequence of snapshots of the moving object. The system is able to capture a single, nonrepetitive event at up to 100 billion frames per second with up to 350 frames per acquisition. The authors have beautifully demonstrated its performance by imaging the propagation of a laser pulse in different materials, its reflection at a mirror, and its refraction at a glass interface, including others.

3 In-Situ Process Monitoring in Technological Laser Processing Applications

Industrial applications of advanced laser processing have been boosted by the widespread availability of Yb-based fiber lasers, reaching 100 s of μJ pulse energies, at 10s of MHz repetition rates and average powers well exceeding 100 W [157]. Chapter 26 provides a detailed view regarding ultra-rapid industrial large area processing by different approaches. While the wealth and potential of the different in-situ probing techniques discussed in the previous sections is without doubt enormous, their application to real-world industrial laser processing is still in its infancy. The major handicaps preventing their widespread use are experimental complexity, slow feedback, and lack of automation. However, some of the techniques have been successfully implemented for industrial processing, and a few examples are given in the next sections.

3.1 Specificity in Laser Cleaning and Art Restauration

Laser cleaning aims at the removal of contaminant particles or layers, which represents a major challenge in several industrial fields [158]. Removal of graffiti from

walls is probably the most well-known application in which dedicated companies offer their service since long. The relative simplicity of this particular application is given by the self-regulation principle: in most cases the contaminating layer absorbs the laser light stronger than the uncontaminated material, which causes the removal process to stop automatically without supervision or control. However, most other laser cleaning applications require a real-time control of the removal process in order to avoid damage of the underlying material.

A particularly relevant sector is art restauration, in which unwanted damage needs to be avoided. Here, laser-induced breakdown spectroscopy (LIBS, see Sect. 2.1) has found its way due to the simple experimental configuration. Employing moderate power lasers, compact fiber optic spectrometers, and raster scanning optics, automatic data acquisition and real-time spectral analysis is possible. The beauty of the technique is that it inflicts minimal damage and not only provides the spectral fingerprint of the contaminated material but also of the underlying material to be preserved, enabling authentication, dating, and conservation in cultural heritage and archaeology [159]. Yet, it is vital to identify the optimum laser cleaning methodology/parameters for a given material, in order to prevent unwanted side effects to occur, such as darkening [160].

3.2 Monitoring the Depth and Side Wall Smoothness in Laser Drilling

Laser drilling of different materials has been implemented in the industry for decades. While drilling with ultrafast lasers is still not widespread due to the much higher photon cost, the unique properties of ultrashort laser pulses enable the fabrication of structures with much higher precision and nanometer size and in transparent materials that cannot be processed with longer pulse lasers [161, 162]. Real-time control of the hole features during the drilling process is therefore of strong interest for industry in order to ensure maximum efficiency and precision. In 2005, Kamiya et al. introduced simple real-time monitoring method to quantify the hole depth during femtosecond laser drilling by analyzing the interference between the processing pulse reflected from sample material and a reference pulse in a Mach-Zehnder interferometer [163]. The depth resolution depends on the laser bandwidth and was 5.5 micrometers in their case.

Another method to quantify the ablation rate is based on a side view configuration (see Sect. 2.5), as reported, for instance, in [164] for a transparent material. The advantage of this approach is the simultaneous monitoring of the side walls (at least in one plane), that is, how conical the shape of the hole becomes. Döring and coauthors [165] demonstrated that this approach can also be used for some semiconductors, using an illumination source at 1060 nm to image the evolution of the hole shape and depth during percussion drilling in silicon. A further advantage of the shadowgraphy approach is the access to transient plasma dynamics, which

provides a means for processing parameter optimization. However, this approach is only valid for materials that offer a transparency regime that allows real-time imaging.

In the context of image-based monitoring of femtosecond laser machining, strong effort is being made by many groups to develop feedback algorithms in order to compensate for laser energy fluctuations or surface layers of unknown thickness (rust). Ideally, an approach without the need to model complex laser-matter interaction process is needed, operating purely with pattern recognition. Mills et al. have introduced a machine learning algorithm based on a neural network that was trained to determine the particular laser parameters that led to optimized ablation of nickel and fused silica samples [166].

Other strategies for real-time monitoring of hole drilling are based on LIBS. Asimellis et al. [167] reported a near-real-time method to determine the layer thickness on electroplated coin blanks during the drilling process via monitoring relative emission-line intensities from key probe elements via successive laser ablation pulses. A similar strategy has been applied to a very different field, laser surgery. Huang and co-workers achieved real-time identification of different tissue types by employing LIBS and spectral recognition algorithms [168]. Their system provides a powerful surgical tool for precise microsurgery applications with real-time feedback.

3.3 Welding Quality Control

Undoubtedly, one of the most important industrial applications of laser materials processing has been metal welding. A large number of publications have described different online monitoring techniques. The more conventional systems use acoustic waves, photo-detectors sensitive in different spectral regions [169], in-situ imaging with CCD or CMOS cameras, pyrometers, or plasma charge sensors [170]. Advanced layouts may include a combination of optical wavelength selective point-probing sensors and spectrometers, UV-visible imaging, high-speed imaging [171], and even X-ray imaging systems [172] as shown in Fig. 7.18. In the case of X-rays, synchrotron-based ultrahigh-speed imaging has also been used to quantify the phenomenon of "keyhole" formation during laser melting of metals [173]. Also recently, optical coherence tomography has been used to monitor in-situ the surface topography of the processing zone, as well as the surrounding area during laser welding [174].

Unlike metals, in the case of glasses, the need for ultrafast lasers for welding is a must due to their optical properties. The first work on glass welding dates back to the early 2000s [175], although the realization of industrially compatible approaches required the further development of high repetition rate Yb-based lasers [176]. Indeed, these sources have enabled a wealth of in-situ imaging pump-probe techniques for industrial processing, as shown in [177]. Among them, pump-probe imaging has been successfully used in laser glass welding [178] and also in glass

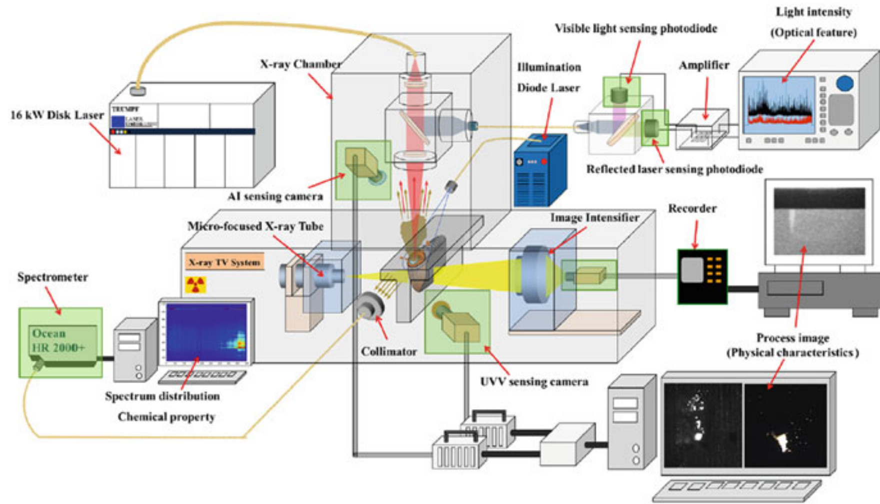

Fig. 7.18 Experimental setup of the measurement system based on multiple sensors during laser welding. (Reprinted with permissions from [172] © Elsevier)

processing approaches involving spatial and temporal shaping of the processing lasers [179].

4 Outlook

The field of probing matter with light during the interaction of a laser pulse with a material system is vast, and this chapter can only give a glimpse of the exciting work performed by a steadily growing scientific community. For obvious space limitation reasons, it is not possible to cite in this review chapter every possible work related to this broad subject, and for sure there are many non-deliberate omissions in it. Still, the subtitle of this book, *The Pursuit of Extreme Scales*, deserves a few additional comments on the exploration of the limits in the spatial and temporal domains.

The impressive advances reached in the field of near field microscopy (and their related local spectroscopies) has enabled the achievement of imaging at spatial resolutions in the few nm to tens of nm range, depending on the approach used (aperture or apertureless scanning near-field optical microscopy, SNOM) [180]. The combination of ad hoc tip fabrication methodologies [181] and the use of adaptive approaches [182] has enabled reaching extreme spatial resolutions also in the so-called tip-enhanced nano-spectroscopies [183]. At the same time, this has enabled reaching extreme enhancement values in tip-enhanced photoluminescence (TEPL) and tip-enhanced Raman spectroscopy (TERS).

The combination of ultrashort laser pulses and light localization phenomena appears therefore as a natural way to move toward higher spatial and temporal resolution limits during the study of light-matter interactions using light probes. Indeed, such a combination has found an ever-increasing number of fundamentally relevant applications that go well beyond the development of fs-resolution, time-resolved SNOM [184, 185]. As described by Lienau and coworkers in ref. [186], "When illuminating metallic nanostructures with ultrashort, femtosecond light pulses, local field intensities are easily reached that are sufficient to generate high harmonic radiation or to propel electrons out of these particles, generating new nanoscale sources of femtosecond electron bunches of potential interest for future applications in ultrahigh time resolution electron microscopy or diffraction [. . .]. Hybrid nanostructures, comprising metals, semiconductors and/or molecular aggregates may find entirely new applications in ultrafast switching or for designing new classes of photonic transistors with unprecedented sensitivity [. . .]." This kind of interactions have led to the relatively recent development of the so-called strong field nano-optics [187] with extremely relevant applications, including the development of new types of ultrafast electron microscopes with unprecedented spatial, temporal, and energy resolution.

With regard to the latter application, along with the combination of light localization phenomena with ultrashort laser pulses, one can naturally think of combining pulsed electron bunches with ultrafast lasers to image the morphological/structural evolution of a laser-excited material at extreme spatial and temporal scales. While this idea is not new at all, and although it does not involve probing matter by light but with electrons, the relation of it with fast and ultrafast laser sources is strong. The first works aimed at developing a "time-resolved" transmission electron microscope using pulsed electron and laser sources date from the early 2000s with the pioneering works by Bostanjoglo [188]. Only 10 years later, the so-called 4D electron microscopy [189] was a reality, and several works have already shown electron imaging and diffraction with temporal resolution in the 100 s of fs range [190–192]. The advances, challenges, and perspectives of 4D electron microscopy have been recently reviewed in ref. [193], with the prospect of achieving Å–fs–meV resolution in the future.

All these recent advances in the development of time-resolved probing with light and electron sources will strongly contribute to unravel the underlying mechanisms of complex interaction pathways. Thanks to this steady growth, combined with decreasing equipment costs and increasing interest of the different technology sectors, the future of in-situ process monitoring for fundamental research and real-world applications is bright. We can certainly expect that nanostructuring with ultrafast lasers will strongly benefit from the increasing capabilities of in-situ monitoring techniques.

References

1. W.M. Steen, J. Mazumder, *Laser Material Processing* (Springer, London, 2010)
2. G.R. Fowles, *Introduction to Modern Optics* (Dover Publications, 1975)
3. R.W. Boyd, *Nonlinear Optics* (Academic Press, 2008)
4. F. Krausz, T. Brabec, Rev. Mod. Phys. **72**, 545 (2000)
5. L.V. Keldysh, Sov. Phys. JETP **20**, 1307 (1965)
6. B. Stuart, M. Feit, S. Herman, A. Rubenchik, B. Shore, M. Perry, Phys. Rev. B Condens. Matter **53**, 1749 (1996)
7. B. Rethfeld, Phys. Rev. B **73**, 035101 (2006)
8. R.W. Boyd, G.L. Fischer, Encycl. Mater. Sci. Technol. Second Ed, 6237 (2001)
9. S.S. Mao, F. Quéré, S. Guizard, X. Mao, R.E. Russo, G. Petite, P. Martin, 1695 (2004). Appl. Phys. A Mater. Sci. Process. **797**, 79 (2004)
10. F. Quéré, S. Guizard, P. Martin, G. Petite, O. Gobert, P. Meynadier, M. Perdrix, Appl. Phys. B Lasers Opt. **68**, 459 (1999) 1999 683
11. M. Garcia-Lechuga, L. Haahr-Lillevang, J. Siegel, P. Balling, S. Guizard, J. Solis, Phys. Rev. B **95**, 214114 (2017)
12. E.G. Gamaly, A.V. Rode, Prog. Quantum Electron. **37**, 215 (2013)
13. M. Gaft, R. Reisfeld, G. Panczer, *Modern Luminescence Spectroscopy of Minerals and Materials* (Springer-Verlag, Berlin/Heidelberg, 2005)
14. R.R. Jones, D.C. Hooper, L. Zhang, D. Wolverson, V.K. Valev, Nanoscale Res. Lett. **14**, 231 (2019)
15. F. Abelès, M.L. Thèye, Surf. Sci. **5**, 325 (1966)
16. J. Hernandez-Rueda, J. Siegel, M. Garcia-Lechuga, J. Solis, J. Opt. Soc. Am. B **31**, 1676 (2014)
17. Q. Li, M. Chambonneau, M. Chanal, D. Grojo, Appl. Opt. **55**, 9577 (2016)
18. W.R. Sooy, M. Geller, D.P. Bortfeld, Appl. Phys. Lett. **5**, 54 (1964)
19. D.A. Cremers, L.J. Radziemski, *Handbook of Laser-Induced Breakdown Spectroscopy*, 2nd edn. (Wiley, 2013)
20. J. Debras-Guédon, N. Liodec, Comptes Rendus l'Académie Des Sci. **257**, 3336 (1963)
21. E.F. Runge, R.W. Minck, F.R. Bryan, Spectrochim. Acta **20**, 733 (1964)
22. S. Legnaioli, B. Campanella, F. Poggialini, S. Pagnotta, M.A. Harith, Z.A. Abdel-Salam, V. Palleschi, Anal. Methods **12**, 1014 (2020)
23. F.J. Gordillo-Vázquez, A. Perea, J.A. Chaos, J. Gonzalo, C.N. Afonso, Appl. Phys. Lett. **78**, 7 (2001)
24. J. Siegel, G. Epurescu, A. Perea, F.J. Gordillo-Vázquez, J. Gonzalo, C.N. Afonso, Spectrochim. Acta - Part B At. Spectrosc. **60**, 915 (2005)
25. J. Siegel, G. Epurescu, A. Perea, F.J. Gordillo-Vázquez, J. Gonzalo, C.N. Afonso, Opt. Lett. **29**, 2228 (2004)
26. G. Epurescu, J. Siegel, J. Gonzalo, F.J. Gordillo-Vázquez, C.N. Afonso, Appl. Phys. Lett. **87**, 1 (2005)
27. J. Squier, D. Harter, F. Salin, G. Mourou, Opt. Lett. **16**, 324 (1991)
28. C. W. White (ed.), *Laser and Electron Beam Processing of Superconductors*, 1st edn. (Academic Press, Orlando, 1980)
29. Y. R. T. Wood, R. F, C. W. White (eds.), *Laser Part. Beams*, vol 4 (1986), p. 321
30. P. Baeri, S.U. Campisano, G. Foti, E. Rimini, Appl. Phys. Lett. **33**, 137 (1978)
31. I.B. Khaibullin, E.I. Shtyrkov, M.M. Zaripov, M.F. Galyautdinov, G.G. Zakirov, Sov. Phys. Semicond. **11**, 190 (1977)
32. D.H. Auston, C.M. Surko, T.N.C. Venkatesan, R.E. Slusher, J.A. Golovchenko, Appl. Phys. Lett. **33**, 437 (1978)
33. D.H. Lowndes, R.F. Wood, Appl. Phys. Lett. **38**, 971 (1981)
34. M.I. Nathan, R.T. Hodgson, E.J. Yoffa, Appl. Phys. Lett. **36**, 512 (1980)
35. D.H. Lowndes, Phys. Rev. Lett. **48**, 267 (1982)

36. H.W. Lo, A. Compaan, Phys. Rev. Lett. **44**, 1604 (1980)
37. K. Murakami, H. Itoh, K. Takita, K. Masuda, Phys. B+C **117–118**, 1024 (1983)
38. D.H. Lowndes, G.E. Jellison, R.F. Wood, Phys. Rev. B **26**, 6747 (1982)
39. G.E. Jellison, D.H. Lowndes, Appl. Phys. Lett. **51**, 352 (1987)
40. R.S. Becker, G.S. Higashi, J.A. Golovchenko, Phys. Rev. Lett. **52**, 307 (1984)
41. D.M.B.C. Larson, C.W. White, T. S. Noggle **48**, 337 (1982)
42. K. Murakami, H.C. Gerritsen, H. van Brug, F. Bijkerk, F.W. Saris, M.J. van der Wiel, Phys. Rev. Lett. **56**, 655 (1986)
43. G.J. Galvin, M.O. Thompson, J.W. Mayer, R.B. Hammond, N. Paulter, P.S. Peercy, Phys. Rev. Lett. **48**, 33 (1982)
44. G.J. Galvin, M.O. Thompson, J.W. Mayer, P.S. Peercy, R.B. Hammond, N. Paulter, Phys. Rev. B **27**, 1079 (1983)
45. R.F. Wood, G.E. Giles, Phys. Rev. B **23**, 2923 (1981)
46. R.F. Wood, J.R. Kirkpatrick, G.E. Giles, Phys. Rev. B **23**, 5555 (1981)
47. J.A. Van Vechten, R. Tsu, F.W. Saris, D. Hoonhout, Phys. Lett. A **74**, 417 (1979)
48. J.A. Van Vechten, R. Tsu, F.W. Saris, Phys. Lett. A **74**, 422 (1979)
49. M.O. Thompson, J.W. Mayer, A.G. Cullis, H.C. Webber, N.G. Chew, J.M. Poate, D.C. Jacobson, Phys. Rev. Lett. **50**, 896 (1983)
50. J. Solis, C.N. Afonso, J. Appl. Phys. **69**, 2105 (1991)
51. T. Sameshima, S. Usui, J. Appl. Phys. **74**, 6592 (1993)
52. J.J.P. Bruines, R.P.M. Van Hal, H.M.J. Boots, W. Sinke, F.W. Saris, Appl. Phys. Lett. **48**, 1252 (1986)
53. J. Siegel, J. Solis, C.N. Afonso, F. Vega, J. Bankmann, O. Martínez Sacristán, K. Sokolowski-Tinten, J. Appl. Phys. **89**, 3642 (2001)
54. M.O. Thompson, G.J. Galvin, J.W. Mayer, P.S. Peercy, J.M. Poate, D.C. Jacobson, A.G. Cullis, N.G. Chew, Phys. Rev. Lett. **52**, 2360 (1984)
55. F. Vega, N. Chaoui, J. Solis, J. Armengol, C.N. Afonso, J. Appl. Phys. **97**, 103519 (2005)
56. S.R. Stiffler, M.O. Thompson, P.S. Peercy, Phys. Rev. B **43**, 9851 (1991)
57. J. Boneberg, P. Leiderer, Phys. Status Solidi Appl. Res. **166**, 643 (1998)
58. M. Wuttig, N. Yamada, Nat. Mater. **6**, 824 (2007)
59. M. Le Gallo, A. Sebastian, J. Phys. D. Appl. Phys. **53**, 213002 (2020)
60. C.J. van der Poel, J. Mater. Res. **3**, 126 (1988)
61. C.N. Afonso, J. Solis, F. Catalina, C. Kalpouzos, Appl. Phys. Lett. **60**, 3123 (1992)
62. J. Siegel, J. Solis, C.N. Afonso, Appl. Surf. Sci. **154**, 130 (2000)
63. Y. Kanemitsu, H. Kuroda, S. Shionoya, Jpn. J. Appl. Phys. **23**, 618 (1984)
64. J. Solis, J. Siegel, C.N. Afonso, Rev. Sci. Instrum. **71**, 1595 (2000)
65. J. Bonse, S.M. Wiggins, J. Solis, J. Appl. Phys. **96**, 2352 (2004)
66. J. Siegel, C.N. Afonso, J. Solis, Appl. Phys. Lett. **75**, 3102 (1999)
67. J. Siegel, A. Schropp, J. Solis, C.N. Afonso, M. Wuttig, Appl. Phys. Lett. **84**, 2250 (2004)
68. S. Wen, Y. Meng, M. Jiang, Y. Wang, Sci. Rep. **8**, 4979 (2018)
69. S. Abdollahramezani, O. Hemmatyar, H. Taghinejad, A. Krasnok, Y. Kiarashinejad, M. Zandehshahvar, A. Alù, A. Adibi, Nanophotonics **9**, 1189 (2020)
70. N. Casquero, Y. Fuentes-Edfuf, R. Zazo, J. Solis, J. Siegel, J. Phys. D. Appl. Phys. **53**, 9 (2020)
71. M. Alvarez-Alegria, J. Siegel, M. Garcia-Pardo, F. Cabello, J. Toudert, E. Haro-Poniatowski, R. Serna, Adv. Opt. Mater. **10**, 2101405 (2022)
72. A.H. Zewail, J. Phys. Chem. A **104**, 5660 (2000)
73. G.A. Mourou, T. Tajima, S.V. Bulanov, Rev. Mod. Phys. **78**, 309 (2006)
74. P.H. Bucksbaum, Science (80-.) **317**, 766 (2007)
75. A. Nayak, M. Dumergue, S. Kühn, S. Mondal, T. Csizmadia, N.G. Harshitha, M. Füle, M. Upadhyay Kahaly, B. Farkas, B. Major, V. Szaszkó-Bogár, P. Földi, S. Majorosi, N. Tsatrafyllis, E. Skantzakis, L. Neoričić, M. Shirozhan, G. Vampa, K. Varjú, P. Tzallas, G. Sansone, D. Charalambidis, S. Kahaly, Phys. Rep. **833**, 1 (2019)
76. M.C. Downer, R.L. Fork, C.V. Shank, J. Opt. Soc. Am. B **2**, 595 (1985)

77. K. Sokolowski-Tinten, J. Bialkowski, M. Boing, A. Cavalleri, D. von der Linde, Phys. Rev. B **58**, R11805 (1998)
78. S. L. Shapiro (ed.), *Ultrashort Light Pulses* (Springer, Berlin Heidelberg, 1977)
79. C.V. Shank, Science **219**, 1027 (1983)
80. A. Brodeur, S.L. Chin, Phys. Rev. Lett. **80**, 4406 (1998)
81. C.V. Shank, R. Yen, C. Hirlimann, Phys. Rev. Lett. **50**, 454 (1983)
82. C.V. Shank, R. Yen, C. Hirlimann, Phys. Rev. Lett. **51**, 900 (1983)
83. P. Saeta, J.-K. Wang, Y. Siegal, N. Bloembergen, E. Mazur, Phys. Rev. Lett. **67**, 1023 (1991)
84. K. Sokolowski-Tinten, J. Bialkowski, D. von der Linde, Phys. Rev. B **51**, 14186 (1995)
85. K. Sokolowski-Tinten, J. Solis, J. Bialkowski, J. Siegel, C.N. Afonso, D. von der Linde, *Tech. Dig. 1998 EQEC. Eur. Quantum Electron. Conf. (Cat. No.98TH8326)* (IEEE, 1998), p. 234
86. J. Solis, C. Afonso, S. Hyde, N. Barry, P. French, Phys. Rev. Lett. **76**, 2519 (1996)
87. D.H. Auston, C.V. Shank, Phys. Rev. Lett. **32**, 1120 (1974)
88. S. Richter, M. Rebarz, O. Herrfurth, S. Espinoza, R. Schmidt-Grund, J. Andreasson, Rev. Sci. Instrum. **92**, 033104 (2021)
89. J.P. Callan, A.M.-T. Kim, L. Huangt, E.N. Glezer, E. Mazur, MRS Online Proc. Libr. **481**, 395 (1997)
90. C.A.D. Roeser, A.M.-T. Kim, J.P. Callan, L. Huang, E.N. Glezer, Y. Siegal, E. Mazur, Rev. Sci. Instrum. **74**, 3413 (2003)
91. L. Huang, J.P. Callan, E.N. Glezer, E. Mazur, Phys. Rev. Lett. **80**, 185 (1998)
92. J.P. Callan, A.M.-T. Kim, C.A.D. Roeser, E. Mazur, J. Solis, J. Siegel, C.N. Afonso, J.C.G. de Sande, Phys. Rev. Lett. **86**, 3650 (2001)
93. A.H. Chin, R.W. Schoenlein, T.E. Glover, P. Balling, W.P. Leemans, C.V. Shank, Phys. Rev. Lett. **83**, 336 (1999)
94. C.W. Siders, A. Cavalleri, K. Sokolowski-Tinten, C. Tóth, T. Guo, M. Kammler, M. Horn Von Hoegen, K.R. Wilson, D. Von Der Linde, C.P.J. Barty, Science (80-.) **286**, 1340 (1999)
95. T. Frigge, B. Hafke, T. Witte, B. Krenzer, C. Streubühr, A. Samad Syed, V. Mikšić Trontl, I. Avigo, P. Zhou, M. Ligges, D. Von Der Linde, U. Bovensiepen, M. Horn-Von Hoegen, S. Wippermann, A. Lücke, S. Sanna, U. Gerstmann, W.G. Schmidt, Nature **544**, 207 (2017)
96. C. Giannetti, M. Capone, D. Fausti, M. Fabrizio, F. Parmigiani, D. Mihailovic, Adv. Phys. **65**, 58 (2016)
97. H.A. Hafez, X. Chai, A. Ibrahim, S. Mondal, D. Férachou, X. Ropagnol, T. Ozaki, J. Opt. **18**, 093004 (2016)
98. M.B. Johnston, L.M. Herz, Acc. Chem. Res. **49**, 146 (2016)
99. J. Hernandez-Rueda, A. Savoia, W. Gawelda, J. Solis, B. Mansart, D. Boschetto, J. Siegel, Appl. Phys. Lett. **98**, 251906 (2011)
100. P. Beaud, S.L. Johnson, A. Streun, R. Abela, D. Abramsohn, D. Grolimund, F. Krasniqi, T. Schmidt, V. Schlott, G. Ingold, Phys. Rev. Lett. **99**, 174801 (2007)
101. M. Forst, T. Dekorsy, C. Trappe, M. Laurenzis, H. Kurz, B. Béchevet, Appl. Phys. Lett. **77**, 1964 (2000)
102. N. Stojanovic, D. von der Linde, K. Sokolowski-Tinten, U. Zastrau, F. Perner, E. Förster, R. Sobierajski, R. Nietubyc, M. Jurek, D. Klinger, J. Pelka, J. Krzywinski, L. Juha, J. Cihelka, A. Velyhan, S. Koptyaev, V. Hajkova, J. Chalupsky, J. Kuba, T. Tschentscher, S. Toleikis, S. Düsterer, H. Redlin, E. Förster, R. Sobierajski, R. Nietubyc, M. Jurek, D. Klinger, J. Pelka, J. Krzywinski, L. Juha, J. Cihelka, A. Velyhan, S. Koptyaev, V. Hajkova, J. Chalupsky, J. Kuba, T. Tschentscher, S. Toleikis, S. Düsterer, H. Redlin, Appl. Phys. Lett. **89**, 89 (2006)
103. M.C. Downer, R.L. Fork, C.V. Shank, *Ultrafast Phenom. IV* (Springer, Berlin, Heidelberg, 1984), pp. 106–110
104. D. von der Linde, K. Sokolowski-Tinten, Appl. Surf. Sci. **154–155**, 1 (2000)
105. K. Sokolowski-Tinten, J. Bialkowski, A. Cavalleri, D. von der Linde, A. Oparin, J. Meyer-ter-Vehn, S. Anisimov, Phys. Rev. Lett. **81**, 224 (1998)
106. D. von der Linde, K. Sokolowski-Tinten, J. Bialkowski, Appl. Surf. Sci. **109–110**, 1 (1997)
107. K. Sokolowski-Tinten, J. Solis, J. Bialkowski, J. Siegel, C.N. Afonso, D. von der Linde, Phys. Rev. Lett. **81**, 3679 (1998)

108. J. Siegel, W. Gawelda, D. Puerto, C. Dorronsoro, J. Solis, C.N. Afonso, J.C.G. De Sande, R. Bez, A. Pirovano, C. Wiemer, J. Appl. Phys. **103**, 023516 (2008)
109. D. Puerto, J. Siegel, W. Gawelda, M. Galvan-Sosa, L. Ehrentraut, J. Bonse, J. Solis, J. Opt. Soc. Am. B **27**, 1065 (2010)
110. J. Hernandez-Rueda, D. Puerto, J. Siegel, M. Galvan-Sosa, J. Solis, Appl. Surf. Sci. **258**, 9389 (2012)
111. M. Garcia-Lechuga, J. Solis, J. Siegel, Appl. Phys. A Mater. Sci. Process. **124**, 221 (2018)
112. M. Garcia-Lechuga, J. Siegel, J. Hernandez-Rueda, J. Solis, Appl. Phys. Lett. **105**, 112902 (2014)
113. P. Kühler, D. Puerto, M. Mosbacher, P. Leiderer, F.J.G. de Abajo, J. Siegel, J. Solis, Beilstein J. Nanotechnol. **4**, 501 (2013)
114. M. Garcia-Lechuga, J. Solis, J. Siegel, Appl. Phys. Lett. **108**, 171901 (2016)
115. M. Garcia-Lechuga, D. Puerto, Y. Fuentes-Edfuf, J. Solis, J. Siegel, ACS Photonics **3**, 1961 (2016)
116. T. Winkler, L. Haahr-Lillevang, C. Sarpe, B. Zielinski, N. Götte, A. Senftleben, P. Balling, T. Baumert, Nat. Phys. **14**, 74 (2018)
117. C. Pan, L. Jiang, J. Sun, Q. Wang, F. Wang, K. Wang, Y. Lu, Y. Wang, L. Qu, T. Cui, Light Sci. Appl. **9**, 80 (2020)
118. C. Xie, R. Meyer, L. Froehly, R. Giust, F. Courvoisier, Light Sci. Appl. **10**, 126 (2021)
119. X.Y. Wang, M.C. Downer, Opt. Lett. **17**, 1450 (1992)
120. S. Rapp, M. Kaiser, M. Schmidt, H.P. Huber, Opt. Express **24**, 17572 (2016)
121. J. Winter, S. Rapp, M. Spellauge, C. Eulenkamp, M. Schmidt, H.P. Huber, Appl. Surf. Sci. **511**, 145514 (2020)
122. J. Winter, S. Rapp, M. Schmidt, H.P. Huber, Appl. Surf. Sci. **417**, 2 (2017)
123. S.H. Møller, S.T. Andersen, P. Balling, Phys. Rev. Res. **2**, 043010 (2020)
124. V.V. Temnov, K. Sokolowski-Tinten, P. Zhou, D. von der Linde, Appl. Phys. A Mater. Sci. Process. **78**, 483 (2004)
125. V.V. Temnov, K. Sokolowski-Tinten, P. Zhou, D. von der Linde, J. Opt. Soc. Am. B **23**, 1954 (2006)
126. L. Gallais, S. Monneret, Opt. Lett. **41**, 3245 (2016)
127. P. Bon, G. Maucort, B. Wattellier, S. Monneret, Opt. Express **17**, 13080 (2009)
128. P. Audebert, P. Daguzan, A. Dos Santos, J.C. Gauthier, J.P. Geindre, S. Guizard, G. Hamoniaux, K. Krastev, P. Martin, G. Petite, A. Antonetti, Phys. Rev. Lett. **73**, 1990 (1994)
129. J.P. Geindre, A. Mysyrowicz, A. Dos Santos, P. Audebert, A. Rousse, G. Hamoniaux, A. Antonetti, F. Falliès, J.C. Gauthier, Opt. Lett. **19**, 1997 (1994)
130. K.J. Wædegaard, D.B. Sandkamm, A. Mouskeftaras, S. Guizard, P. Balling, Europhys. Lett. **105**, 47001 (2014)
131. A. Mouskeftaras, S. Guizard, N. Fedorov, S. Klimentov, Appl. Phys. A Mater. Sci. Process. **110**, 709 (2013)
132. D. Puerto, W. Gawelda, J. Siegel, J. Bonse, G. Bachelier, J. Solis, Appl. Phys. A Mater. Sci. Process. **92**, 803 (2008)
133. W. Gawelda, D. Puerto, J. Siegel, A. Ferrer, A.R. De La Cruz, H. Fernández, J. Solis, Appl. Phys. Lett. **93**, 93 (2008)
134. F. Wang, C. Pan, J. Sun, Q. Wang, Y. Lu, L. Jiang, Opt. Express **27**, 10050 (2019)
135. Q. Sun, H. Jiang, Y. Liu, Z. Wu, H. Yang, Q. Gong, Opt. Lett. **30**, 320 (2005)
136. A. Mermillod-Blondin, J. Bonse, A. Rosenfeld, I.V. Hertel, Y.P. Meshcheryakov, N.M. Bulgakova, E. Audouard, R. Stoian, Appl. Phys. Lett. **94**, 041911 (2009)
137. A. Mouskeftaras, M. Chanal, M. Chambonneau, R. Clady, O. Utéza, D. Grojo, Appl. Phys. Lett. **108**, 41107 (2016)
138. H. Hu, X. Wang, H. Zhai, N. Zhang, P. Wang, Appl. Phys. Lett. **97**, 061117 (2010)
139. A. Vogel, I. Apitz, S. Freidank, R. Dijkink, Opt. Lett. **31**, 1812 (2006)
140. L. Gao, J. Liang, C. Li, L.V. Wang, Nature **516**, 74 (2014) 5167529
141. B. Guo, J. Sun, Y.F. Lu, L. Jiang, Int. J. Extrem. Manuf. **1**, 032004 (2019)

142. B. Guo, *Handb. Laser Micro-Nano-Engineering* (Springer International Publishing, Cham, 2020), pp. 1–51
143. J. Liang, L.V. Wang, Opt **5**(9), 1113–1127 (2018)
144. H. Mikami, L. Gao, K. Goda, Nanophotonics **5**, 441 (2016)
145. P.R. Poulin, K.A. Nelson, Science (80-.) **313**, 1756 (2006)
146. T. Shin, J.W. Wolfson, S.W. Teitelbaum, M. Kandyla, K.A. Nelson, Rev. Sci. Instrum. **85**, 083115 (2014)
147. X. Wang, L. Yan, J. Si, S. Matsuo, H. Xu, X. Hou, Appl. Opt. **53**, 8395 (2014)
148. K. Nakagawa, A. Iwasaki, Y. Oishi, R. Horisaki, A. Tsukamoto, A. Nakamura, K. Hirosawa, H. Liao, T. Ushida, K. Goda, F. Kannari, I. Sakuma, Nat. Photonics **8**, 6 (2014)
149. T. Suzuki, R. Hida, Y. Yamaguchi, K. Nakagawa, T. Saiki, F. Kannari, Appl. Phys. Express **10**, 092502 (2017)
150. X. Zeng, S. Zheng, Y. Cai, Q. Lin, J. Liang, X. Lu, J. Li, W. Xie, S. Xu, Adv. Photonics **2**, 1 (2020)
151. C. Li, G. Cheng, X. Sedao, W. Zhang, H. Zhang, N. Faure, D. Jamon, J.-P. Colombier, R. Stoian, Opt. Express **24**, 11558 (2016)
152. Z. Li, R. Zgadzaj, X. Wang, Y.-Y. Chang, M.C. Downer, Nat. Commun. **5**, 3085 (2014)
153. A. Ehn, J. Bood, Z. Li, E. Berrocal, M. Aldén, E. Kristensson, Light Sci. Appl. **6**, e17045 (2017)
154. M.A.A. Neil, R. Juškaitis, T. Wilson, Opt. Lett. **22**, 1905 (1997)
155. M.J. Cole, J. Siegel, S.E. Webb, R. Jones, K. Dowling, P.M. French, M.J. Lever, L.O. Sucharov, M.A. Neil, R. Juskaitis, T. Wilson, Opt. Lett. **25**, 1361 (2000)
156. Q.-Y. Yue, Z.-J. Cheng, L. Han, Y. Yang, C.-S. Guo, Opt. Express **25**, 14182 (2017)
157. G. Chang, Z. Wei, IScience **23**, 101101 (2020)
158. D.M. Kane, *Laser Cleaning II* (World Scientific Publishing Co, 2007)
159. A. Botto, B. Campanella, S. Legnaioli, M. Lezzerini, G. Lorenzetti, S. Pagnotta, F. Poggialini, V. Palleschi, J. Anal. At. Spectrom. **34**, 81 (2019)
160. P. Pouli, M. Oujja, M. Castillejo, Appl. Phys. A Mater. Sci. Process. **106**, 1062 (2011) 447 (2011)
161. R. Stoian, J.-P. Colombier, Nanophotonics **9**, 4665 (2020)
162. R. Osellame, G. Cerullo, R. Ramponi, *Femtosecond Laser Micromachining* (Springer, Berlin Heidelberg, 2012)
163. M. Kamiya, S. Aoshima, Rev. Laser Eng. **33**, 685 (2005)
164. D. Grossmann, M. Reininghaus, C. Kalupka, M. Jenne, M. Kumkar, Opt. Express **25**, 28478 (2017)
165. S. Döring, S. Richter, S. Nolte, A. Tünnermann, Opt. Express **18**, 20395 (2010)
166. B. Mills, D.J. Heath, J.A. Grant-Jacob, Y. Xie, R.W. Eason, J. Phys. Photonics **1**, 015008 (2018)
167. G. Asimellis, A. Giannoudakos, M. Kompitsas, Appl. Opt. **46**, 935 (2007)
168. H. Huang, L.-M. Yang, S. Bai, J. Liu, J. Biomed. Opt. **20**, 028001 (2015)
169. P. De Bono, C. Allen, G. D'Angelo, A. Cisi, J. Laser Appl. **29**, 022417 (2017)
170. J. Shao, Y. Yan, J. Phys. Conf. Ser. **15**, 101 (2005)
171. S.M. Robertson, A.F.H. Kaplan, J. Frostevarg, J. Manuf. Process. **67**, 91 (2021)
172. D. You, X. Gao, S. Katayama, J. Mater. Process. Technol. **219**, 209 (2015)
173. R. Cunningham, C. Zhao, N. Parab, C. Kantzos, J. Pauza, K. Fezzaa, T. Sun, A.D. Rollett, Science (80-.) **363**, 849 (2019)
174. C. Stadter, M. Schmoeller, M. Zeitler, V. Tueretkan, U. Munzert, M.F. Zaeh, J. Laser Appl. **31**, 022408 (2019)
175. T. Tamaki, W. Watanabe, J. Nishii, K. Itoh, Jpn. J. Appl. Phys. **44**, L687 (2005)
176. S. Richter, S. Döring, A. Tünnermann, S. Nolte, Appl. Phys. A Mater. Sci. Process. **103**, 257 (2011)
177. M. Jenne, F. Zimmermann, D. Flamm, D. Großmann, J. Kleiner, M. Kumkar, S. Nolte, J. Laser Micro Nanoeng. **13**, 273 (2018)

178. A. Gruber, F. Zimmermann, M. Jenne, D.G. Grossmann, M. Kumkar, in *Laser Appl. Microelectron. Optoelectron. Manuf. XXIII*, ed. by B. Neuenschwander, G. Račiukaitis, T. Makimura, C. P. Grigoropoulos, (SPIE, 2018), p. 051906-1–6
179. M. Jenne, D. Flamm, M. Faber, D. Grossmann, J. Kleiner, F. Zimmermann, M. Kumkar, S. Nolte, in *Laser-Based Micro- Nanoprocessing XIII*, ed. by U. Klotzbach, R. Kling, A. Watanabe, (SPIE, 2019), p. 109061G-1–7
180. P. Bazylewski, S. Ezugwu, G. Fanchini, Appl. Sci. **7**, 973 (2017)
181. W.-S. Chang, S. Bauerdick, M.S. Jeong, Ultramicroscopy **108**, 1070 (2008)
182. D.Y. Lee, C. Park, J. Choi, Y. Koo, M. Kang, M.S. Jeong, M.B. Raschke, K.D. Park, Nat. Commun. **12**, 1 (2021)
183. K.D. Park, M.A. May, H. Leng, J. Wang, J.A. Kropp, T. Gougousi, M. Pelton, M.B. Raschke, Sci. Adv. **5**, 1 (2019)
184. R.V. Ovali, R. Sahin, A. Bek, M.E. Tasgin, Appl. Phys. Lett. **118** (2021)
185. M. Wagner, Z. Fei, A.S. McLeod, A.S. Rodin, W. Bao, E.G. Iwinski, Z. Zhao, M. Goldflam, M. Liu, G. Dominguez, M. Thiemens, M.M. Fogler, A.H. Castro Neto, C.N. Lau, S. Amarie, F. Keilmann, D.N. Basov, Nanophotonics Lett. **14**, 894 (2014)
186. C. Lienau, M.A. Noginov, M. Lončar, J. Opt. (United Kingdom) **16**, 13 (2014)
187. P. Dombi, Z. Pápa, J. Vogelsang, S.V. Yalunin, M. Sivis, G. Herink, S. Schäfer, P. Groß, C. Ropers, C. Lienau, Rev. Mod. Phys. **92**, 1 (2020)
188. O. Bostanjoglo, R. Elschner, Z. Mao, T. Nink, M. Weingärtner, Ultramicroscopy **81**, 141 (2000)
189. A.H. Zewail, Science **328**, 187 (2010)
190. D.J. Flannigan, A.H. Zewail, Acc. Chem. Res. **45**, 1828 (2012)
191. L. Piazza, D.J. Masiel, T. LaGrange, B.W. Reed, B. Barwick, F. Carbone, Chem. Phys. **423**, 79 (2013)
192. T. LaGrange, B.W. Reed, M.K. Santala, J.T. McKeown, A. Kulovits, J.M.K. Wiezorek, L. Nikolova, F. Rosei, B.J. Siwick, G.H. Campbell, Micron **43**, 1108 (2012)
193. W.A. Curtis, D.J. Flannigan, Phys. Chem. Chem. Phys. **23**, 23544 (2021)